David A. Egger

Electronic structure of self-assembled monolayers with distributed dipole moments

Masterarbeit

zur Erlangung des akademischen Grades

Diplom-Ingenieur

Masterstudium Technische Physik

Graz University of Technology
Technische Universität Graz

Betreuer:

Ao.Univ.-Prof. Dipl.-Ing. Dr.techn. Egbert Zojer

Institut für Festkörperphysik

Graz, April 2010

Deutsche Fassung:
Beschluss der Curricula-Kommission für Bachelor-, Master- und Diplomstudien vom 10.11.2008
Genehmigung des Senates am 1.12.2008

EIDESSTATTLICHE ERKLÄRUNG

Ich erkläre an Eides statt, dass ich die vorliegende Arbeit selbstständig verfasst, andere als die angegebenen Quellen/Hilfsmittel nicht benutzt, und die den benutzten Quellen wörtlich und inhaltlich entnommene Stellen als solche kenntlich gemacht habe.

Graz, am ……. ……..
(Unterschrift)

Englische Fassung:

STATUTORY DECLARATION

I declare that I have authored this thesis independently, that I have not used other than the declared sources / resources, and that I have explicitly marked all material which has been quoted either literally or by content from the used sources.

……. ……..
date (signature)

Acknowledgments

This thesis and my studies of physics would not have been possible without the support and friendship of many people.

I would like to thank my supervisor Prof. Egbert Zojer for supporting me during my Master's thesis in the last eight months. Amongst many other things, I'm grateful for the extraordinary scientific experiences I could make in this time.

Special thanks to Georg Heimel for fruitful discussions on physics and everything, Italian cuisine in Adlershof and for taking care of me during my visit to Berlin. It certainly was a great time and I could learn a lot! I also would like to thank the group of Prof. Norbert Koch at the Humboldt Universität zu Berlin.

A big thank you to all the members of the Egbert group for the good atmosphere in- and outside the university. I want to thank Ferdinand Rissner for his VASP expertise, a lot of help during 'distributing the dipoles', the brilliant 'heap array' shot and for good spirit when working as a team. Thanks to Gerold Rangger for awk-scripts, introducing me to SIESTA and for riding the bike with me at 6 in the morning; to Oliver Hofmann for chemical advise and help in GAUSSIAN. I also would like to thank Lukas Wittwer for geometries and Anna Track for reminding me of an important paper.

During my studies I was lucky to meet Sebastian Schuh, Andi Schriefl, Max Besenhard and Michael Hörzinger. Your company made the learning, report writing and studying a good thing.

I'm grateful to my best friend Jakob Primosch for being exactly the way he is and just accepting me the way I am - thank you for your friendship and patience whenever I'm busy with whatever might be important to me.

Thanks to my mother Liliane, my father Joe, my grandmother Karoline and my brother Philipp for their love and support over the past years. I want to express my highest gratitude to my parents for how they cared about my brother and me.

Last, but definitely not least, I am deeply indebted to Alexandra for the best time of my life, her spirit when cheering me up, her clear way of thinking whenever I don't see a way out, for being thoughtful when weekends were full of work and for her love over the past years.

David

Abstract

Electronic structure of self-assembled monolayers with distributed dipole moments

David A. Egger
Institute of Solid State Physics, University of Technology, Graz
8010 Graz, Austria

The adsorption of self-assembled monolayers (SAMs) on metal electrodes is well known to enhance the performance of (opto)electronic devices. In detail, polar SAMs were shown to critically influence the work function and electronic structure at the metal/organic interface. Attaching polar groups or changing the docking group of the SAM-forming molecule was discussed as a tuning strategy in that context. In the present work, the impact of polar units built directly into the molecular backbone is investigated. Therefore, slab-type band-structure calculations at the density function theory level are carried out for oligopyrimidines. The resulting polar backbones are compared to SAMs where strong dipole moments are introduced by end-group substitutions. An entirely different evolution of the quantities of interest with the backbone length is found for the two systems. Moreover, a pronounced reduction of the Kohn-Sham gap was found to be the consequence of a collective electrostatic effect present in such a molecular ensemble. Furthermore, electronic transport in a device based on monolayers similar to the aforementioned SAMs is considered. This is done by calculating transmission coefficients applying a Greens function approach to dithiolates bonded to two electrodes. The necessary theoretical and computational knowledge gained during a visit at the Humboldt Universität zu Berlin is reviewed, tested and compared to the literature. For the investigated systems, significant differences in their transport behavior could be observed. They were, however, identified as a consequence of the properties of the isolated SAM-forming molecules. Finally, the the surface-density of states and surface band-structure are of oligopyrimidine SAMs calculated by Green's functions techniques.

Abstrakt

Elektronische Struktur selbst-assemblierter Monolagen mit verteilten Dipolen

David A. Egger
Institut für Festkörperphysik, Technische Universität Graz
8010 Graz, Austria

Die Adsorption selbst-assemblierter Monolagen (SAMs) hat sich als Methode zur Effizienzsteigerung (opto)elektronischer Bauelemente bewährt. Insbesondere konnte mit polaren Monolagen die Austrittsarbeit von Metallelektroden und die elektronische Strukur an der Grenzfläche Metall/organisches-Molekül modifiziert werden. Die Substitution polarer Gruppen an den jeweiligen Enden der SAM wurde in diesem Kontext als Tuning-Strategie diskutiert. In der vorliegenden Arbeit wird nun der Einfluss polarer Gruppen innerhalb der Monolage untersucht. Zu diesem Zweck werden "slab-type"-Bandstrukturrechnungen auf Dichtefunktionalstheorie Niveau für Systeme mit Dipolen entlang der Molekülachse durchgeführt. Diese polaren "Backbones" werden mit ihren Endruppen-substituierten Pendants, deren "Backbones" entsprechend nicht polar sind, verglichen. Hinsichtlich der Evolution physikalischer Observablen mit der Dicke der Monolage wurde zwei vollkommen verschiedene Verläufe gefunden. Darüber hinaus wurde eine prononcierte Reduktion der Bandlücke innerhalb der Monolage als Folge kollektiver elektrostatischen Effekte festgestellt. Weiters wurde der elektronische Transport innerhalb eines Bauelements basierend auf sehr ähnlichen SAMs untersucht. Die dafür notwendigen, während eines Forschungsaufenthalts an der Humboldt Universität zu Berlin erworbenen, theoretischen und programmtechnischen Grundlagen werden vorgestellt, getestet und mit der Literatur verglichen. Für die untersuchten Systeme konnte der Unterschied im Transportverhalten auf die Eigenschaften der jeweiligen Einzelmoleküle zurückgeführt werden. Weiters werden die Konzepte der Oberflächen-Zustandsdichte und Bandstruktur vorgestellt.

Contents

Chapter 1

Introduction

> Those who have handled sciences have been either men of experiment or men of dogmas. The men of experiment are like the ant;they only collect and use:the reasoners resemble spiders, who make cobwebs out of their own substance. But the bee takes the middle course; it gathers its material from the flowers of the garden and of the field, but transforms and digests it by a power of its own.
>
> Francis Bacon[1]

With the spirit of this brilliant aphorism by Francis Bacon the present contribution arrogates to take the role of the bee. Computational solid-state physics, on the edge between theory and experiment, is the topic of this work.

This thesis investigates the electronic properties of self-assembled monolayers(SAMs) adsorbed on metal surfaces. Such monolayers are promising candidates in nanotechnology [2]. In the following, I will overview the contents:

We investigated the electronic structure of SAMS, where dipoles are distributed along the backbone, by means of density functional theory based band-structure calculations. The theoretical basics of electronic structure calculations are summarized in chapter I. We also considered the transport characteristics of monolayers. Calculating electronic transport needs a few elements of many-body theory which are introduced in chapter II.

Chapter III starts with reviewing the microscopic origin of SAM-induced interface modification. There, literature that helped me to understand the energetics of organic monolayers on surfaces, is summarized. Afterwards the methodology of our calculations is listed. Ferdinand Rissner helped me to use the VASP code and enabled me to perform band-structure calculations.

The main topic in chapter III is the distributed dipoles approach. This approach is realized with monolayers of different length built of pyrimidine rings. There, we first investigate how the situation changes when elongating the monolayer. We found a significant difference when comparing those monolayers to head- group substituted biphenylthiols. Those contents were published by David A. Egger, Ferdinand Rissner, Gerold M. Rangger, Oliver T. Hofmann, Lukas Wittwer, Georg Heimel and Egbert Zojer in *Phys.Chem.Chem.Phys.* [3]. Ferdinand Rissner supported me with his knowledge on band-structure calculations and introduced me into computational solid-state physics. His contributions to this section also concerned the interpretation of the results in a profound way. Gerold M. Rangger helped me in understanding and analyzing the obtained results. Oliver T. Hofmann supported this work in fruitful discussions concerning the polarization of such polar molecules. Lukas Wittwer performed a part of the geometry optimization in GADGET. Georg Heimel made significant contributions to the scientific discussion and to the published manuscript. Egbert Zojer contributed frequently to the topic and had the idea of distributing dipoles along the backbone.

The second scientific aspect in chapter III concerns the investigation of the electronic structure of the aforementioned monolayers of polar building blocks. We found the Kohn-Sham gap to be reduced when increasing the packing density. We can relate those findings to a collective electrostatic effect present in such an ensemble of polar molecules. In calculations on the isolated terpyrimidine molecule we found that the ordering of the orbitals depends on the applied functional. That finding may be related to what is known as the self-interaction error of GGA. This part of the thesis was initialized by the fact that the IP on the docking side of the free-standing SAM was changed or remained constant when making the backbone longer, depending on the nitrogen position within the pyrimidine monolayers. That puzzle was resolved by a hypothesis: I suggested that the orbitals are localized in the monolayer. I was introduced to the LDOS by Egbert Zojer and to the RDOS by Ferdinand Rissner. We found the orbitals to be localized in the SAM and the hypothesis was confirmed. After I found that a reduction of the band-gap is the consequence of that localization, we discovered the HOMO to have σ character. Oliver T. Hofmann helped me in performing several calculations in GAUSSIAN. There we found a functional dependent molecular ordering. Leeor Kronik and Amir Natan brought the self-interaction error to my mind during their visit in Graz, Anna M. Track and Anne-Marie Kelterer suggested very helpful publications in this context. We analyzed the coverage dependent electronic structure of those systems in great detail. Here, Ferdinand Rissner was responsible for plotting the LDOS at several coverages and could streamline the scientific aspect of the topic in several discussions. He

also made significant contributions to the present composition of the text.

In chapter IV the possibility of calculating electronic transport on the atomic scale is explored. By means of Green's function techniques we derive a formalism to calculate IV-curves within the DFT framework. The theoretical fundamentals and computational implementation, gained during a visit to the Humboldt Universität zu Berlin, are introduced and explained. The codes are tested and compared with the literature for a device based on biphenyldithiolate. We apply the approach to a device based on a SAM with distributed dipoles and can relate the results to properties of the isolated molecules. Furthermore, preliminary results in terms of the surface DOS and surface band structure are shown. Georg Heimel introduced me into this topic, provided helpful literature and explained the computational implementation. He also had the idea of considering the surface band structure. Egbert Zojer suggested the two monolayers as candidates for electronic transport, participated in several discussions and helped me to perform calculations on the isolated molecule.

Chapter 2

Theory I: Equations of motions for many particles

The problem in theoretical condensed matter physics is to solve the equations of motion for atomic systems. While hydrogen like atoms are indeed "pencil and paper" problems systems constistent of more particles cannot be solved analtytically. The field of solid state theory did invent a handful of clever ways around this unsatisfying situation. Some of them have been applied in this work and are introduced in the following. The content described in the following stems from Refs. [4, 5].

2.1 Decoupled motion of electrons and protons or: the Born-Oppenheimer approximation

The motion of an atom can be described as the motion of its electrons and the positive ions. Those particles behave correlated due to the wide ranging Coloumb interaction. As describing such a correlated motion is a rather complicated problem, Born and Oppenheimer introduced [6] the concept of seperating the motion of the ions and electrons. Instead of one wavefunction describing the behavior of ions and electrons one has two *seperated* wavefunctions, which together represent the total system:

$$\Psi_{\text{total}} = \psi_{electrons} \times \psi_{ions}. \tag{2.1}$$

Figure 2.1 visualizes the Born-Oppenheimer approximation: The ions are *pinned* in space while the electrons "sneak by them" (Felix Bloch) and we solve the equations of motion of the electrons. This at a first glance maybe crude approximation is justified by the fact that the mass of a proton is around 2000 times bigger than the mass of an electron. It is therefore reasonable to make the assumption that the motion of the light electrons does

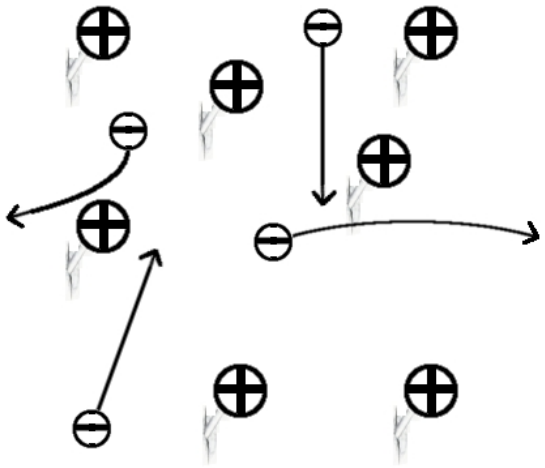

Figure 2.1: *Pinned* positive ions and 'sneaking' electrons within the Born-Oppenheimer approximation

not affect the heavy ions. Thus the motions of electrons and ions are not considered simultaneously but seperated: The nuclear part of the system is kept fix while the electronic equations are solved and vice versa.
We therefore split our approach in two parts. First we will derive how to solve the equations of motion for electrons, and then use the result to find a solution for the ions.

2.2 From 3N to 3 variables - Density functional theory

The challenging part in solving the equations of motion for many electrons is the very large number of variables. The (time-indipendent) many electron problem is described by the corresponding Schrödinger equation:

$$\hat{H}\Psi = \left[\hat{T} + \hat{V} + \hat{U}\right]\Psi = \left[\sum_{i}^{N} -\frac{\hbar^2}{2m}\nabla_i^2 + \sum_{i}^{N} V(\boldsymbol{r}_i) + \sum_{i<j}^{N} U(\boldsymbol{r}_i, \boldsymbol{r}_j)\right]\Psi = \\ = E\Psi. \tag{2.2}$$

Here, $\Psi = \Psi(\boldsymbol{r}_1, \ldots, \boldsymbol{r}_N)$ is a function of $3N$ spatial coordinates (we neglect the N spin coordinates in the discussion of the theoretical basics). Typical physical problems deal with $N = \mathcal{O}(10^{24})$ particles. Thus it is absurd to even think of solving Eq. 2.2 in a straightforward manner.
An elegant pathway to handle this dilemma goes back to the briliant idea of Pierre Hohenberg and Walter Kohn to represent the system by its electron

density $n(\boldsymbol{r})$ [7] (this concept is in fact quite a few years older and was already known as the Thomas-Fermi model [8]). They showed that there is *one unique* ground-state wavefunction $\Psi_0(\boldsymbol{r}_1, \ldots, \boldsymbol{r}_N)$ associated to the ground-state electron density $n_0(\boldsymbol{r})$

$$\Psi_0(\boldsymbol{r}_1, \ldots, \boldsymbol{r}_N) \leftrightarrow n_0(\boldsymbol{r}). \tag{2.3}$$

This argument can be motivated by the fact that the ground-state electron density $n_0(\boldsymbol{r})$ is a functional of the ground-state wavefunction $\Psi_0(\boldsymbol{r}_1, \ldots, \boldsymbol{r}_N)$ itself

$$n_0(\boldsymbol{r}) = n_0[\Psi_0(\boldsymbol{r}_1, \ldots, \boldsymbol{r}_N)] = \langle \Psi_0 | \sum_i^N \delta(\boldsymbol{r} - \boldsymbol{r}_i) | \Psi_0 \rangle . \tag{2.4}$$

Changing the density $n(\boldsymbol{r})$ would change the external potential $\hat{V}$ in Eq. 2.2, which, as Hohenberg and Kohn showed, manifests in a change in the wavefunction of the system. Given an external potential, there is a unique way to get the ground-state electron density n_0 and therefore the ground-state wavefunction Ψ_0! Of course the ground-state energy E_0 is also a functional of the ground-state wavefunction

$$E_0(\boldsymbol{r}) = E_0[\Psi_0(\boldsymbol{r}_1, \ldots, \boldsymbol{r}_N)] = \langle \Psi_0 | \hat{H} | \Psi_0 \rangle . \tag{2.5}$$

In this way Hohenberg and Kohn have mapped the quantity of interest from $3N$ onto three variables. According to what is known as the *Ritz method* [9] one has to solve the variatonal problem

$$\delta E[n(\boldsymbol{r})] = 0 \qquad \text{N.B.} \qquad \int \mathrm{d}^3 r n(\boldsymbol{r}) = N \tag{2.6}$$

to finally arrive at the ground-state wavefunction and energy, the problem is solved!
This is put into perspective by the fact that the complete energy-density functional

$$E[n_0] = V[n_0] + T[n_0] + U[n_0], \tag{2.7}$$

is not known. Only the external potential in Eq. 2.7 can be written straightforward as a functional of the electron density

$$V[n_0] = \int \mathrm{d}^3 r \; v(\boldsymbol{r}) n_0(\boldsymbol{r}), \tag{2.8}$$

the kinetic part $T[n_0]$ and the interaction part $U[n_0]$ in Eq. 2.7 are not that easy to state.
Walter Kohn and Lu Jeu Sham introduced a concept to address this unsatisfying situation [10]. The basic idea of Kohn and Sham is the following:
The interaction part of the Hamiltonian is built containing the Hartree term

of the Hartree-Fock approach (representing the exact local Coloumb interaction) and two unknown parts, namely the exchange and correlation terms:

$$U[n(r)] = \frac{e^2}{2}\int \mathrm{d}^3r \int \mathrm{d}^3r' \frac{n(\boldsymbol{r})n(\boldsymbol{r'})}{|\boldsymbol{r}-\boldsymbol{r'}|} + E_x[n(r)] + E_c[n(r)]. \tag{2.9}$$

$E_x[n(r)]$ and $E_c[n(r)$ remain unknown and one has to use approximations to make use Eq. 2.9. The kinetic part of the full Hamiltonian is approximated by the standard kinetic-energy operator for a Slater-determinant basis:

$$T[n(\boldsymbol{r})] = \sum_i^N \int \mathrm{d}^3r \psi_i^*(\boldsymbol{r})\Big(-\frac{\hbar^2\nabla^2}{2m}\Big)\psi_i(\boldsymbol{r}). \tag{2.10}$$

Here the ψ_i are meant to be the atomic orbitals that constitute the wavefunction by a Slater-determinant. Thus Eq. 2.10 is the kinetic term for *non-interacting* particles. We are of course dealing with interacting particles, so to take the kinetic represantation of non-interacting particles seems to be wrong. But that's the point: Everything that is *beyond* the non-interacting situation was already included in Eq. 2.9, *i.e.* the exchange and correlation terms. We can perform the variational Ansatz, again by using Langrange multipliers to successfully arrive at the famous Kohn-Sham equation:

$$\left[-\frac{\hbar^2}{2m}\nabla_i^2 + v(\boldsymbol{r}) + e^2\int \mathrm{d}^3r' \frac{n(\boldsymbol{r'})}{|\boldsymbol{r}-\boldsymbol{r'}|} + \frac{\delta E_{xc}[n(\boldsymbol{r})]}{\delta n(\boldsymbol{r})}\right]\psi_i(\boldsymbol{r}) = \epsilon_i\psi_i(\boldsymbol{r}). \tag{2.11}$$

Solving equation 2.11 in a self-consistent manner is what is known as density functional theory (DFT). This procedure is in principle exact and without any approximation.
De facto no one knows the analytic expression for $E_{xc}[n(\boldsymbol{r})]$ in Eq. 2.11. Therefore, approximations are essential for practical DFT. Two *state of the art* exchange-correlation functionals were applied throughout this thesis: The PW91 [11] functional implemented in the **VASP** code [12] and the PBE [13] functional implemented in the **SIESTA** code [14]. Both rely on a generalized-gradient approximation (GGA) and depend on the electron density and its gradient at point $\boldsymbol{r}$. Non-local phenomena such as Van der Waals-forces are not treatable within the description of the system by such local functionals.

2.3 Basis sets

Eq. 2.11 implies the need of a proper basis to expand the $\psi_i(\boldsymbol{r})$:

$$\psi_i(\boldsymbol{r}) = \sum_t a_t(\boldsymbol{k})\Phi_{\boldsymbol{k},t}(\boldsymbol{r}). \tag{2.12}$$

The resulting basis functions $\Phi_{\boldsymbol{k},s}(\boldsymbol{r})$ are then called a basis set. To benefit from expressing the wavefunction using a basis set, it has to be finite. Therefore the introduction of a basis set is an approximation. The usual treatment is to think of a solid as an infinite repetition of one unit. We immediately recognize that this reduces the problem from describing the motion of the particles in the whole solid to describing it in just a part of it. The part of the solid to which the problem is reduced to is called unit cell and infinitely expanded in space afterwards. This treatment is realized by periodic boundary conditions; so the physics in the solid has to be same in every unit cell (here we focus on the expectation value of the wavefunction, but of course the potential and any other observable is per definition periodic):

$$|\psi(\boldsymbol{r}+\boldsymbol{R})|^2 = |\psi(\boldsymbol{r})|^2. \tag{2.13}$$

Here $\boldsymbol{R}$ means the unit vector. Felix Bloch in 1936 [15] derived the suitable form of wavefuctions representing this philosophy. He showed that every periodic wavefunction in the sense of Eq. 2.13 has to have the general form:

$$\psi_{\boldsymbol{k}}(\boldsymbol{r}) = u_{\boldsymbol{k}}(\boldsymbol{r})e^{i\boldsymbol{k}\boldsymbol{r}}. \tag{2.14}$$

Those are called *Bloch waves*, Bloch's theorem states that every wavefunction obeying Eq. 2.13 is a plane wave modulated by the lattice periodic function

$$u_{\boldsymbol{k}}(\boldsymbol{r}) = u_{\boldsymbol{k}}(\boldsymbol{r}+\boldsymbol{R}). \tag{2.15}$$

You maybe noted the $\boldsymbol{k}$ indices in Eq. 2.14 and Eq. 2.15 indicating the periodicity in reciprocal space.
We now know how the wavefunction in general has to look like. The two ways to approach this general form applied thoughout this thesis are described in the following.

2.3.1 Plane waves

Plane waves of the general form

$$\Phi_{\boldsymbol{k},s}(\boldsymbol{r}) = \frac{1}{\sqrt{\Omega}}\, e^{i(\boldsymbol{k}+\boldsymbol{K}_s)\cdot\boldsymbol{r}} \tag{2.16}$$

are suitable basis functions for constructing Bloch sets. Is seems not suprising that the more plane waves one takes into account to represent the wavefunction, the more accurate the results get. Thus the plane wave Ansatz relies to high computational effort in order to achieve required accuracy.

2.3.2 Atomic orbitals

One shortcoming of the plane-wave method is that its computational costs scale with N^3, where N is the number of electrons in the system. An atomic-orbital expression [16]

$$\Phi_{\boldsymbol{k}}(\boldsymbol{r}) = \sum_n e^{i\boldsymbol{k}\boldsymbol{R}_n} \Phi_n(\boldsymbol{r} - \boldsymbol{R}_n), \tag{2.17}$$

with Φ_n is an atomic orbital ψ_α, is implemented in the SIESTA code. SIESTA is a linear scaling DFT code where the ψ_α are built of a numerical radial part and spherical harmonics. But the key attribute of this basis set is its locality: The atomic orbitals are localized and there is no 'infinite' long-range interaction in the system. This is an important feature for some problems in condensed matter physics (*vide infra*).

2.4 The link between the seperated motions of electrons and ions - Hellmann-Feynman Theorem

The Born-Oppenheimer approximation meant to keep the ions fixed and solve the Schrödinger equation for the electrons within the DFT framework. Now the influence of the electrons on the ions is needed. Several authors (*e.g.* Wolfgang Pauli, Hans Hellmann, Richard Feynman [17]) indipendently proofed the following Theorem:

$$\frac{\partial E}{\partial \lambda} = \int \psi^*(\lambda) \frac{\partial \hat{H}_\lambda}{\partial \lambda} \psi(\lambda)\, d\tau. \tag{2.18}$$

Eq. 2.18 is known as the Hellmann-Feynman Theorem and states that the derivative of the energy with respect to some variable λ is a functional of the λ-dependent wavefunction. Now if λ is thought to be the vector $\boldsymbol{r}$ and the Hamiltonian and wavefunction are obtained via DFT one can calculate the intra-molecular forces and solve the equations of motions for the ions.
This was carried out by the external optimizer GADGET [18] in internal coordinates (solving the equations of motion in internal coordinates delivered up to 0.3 eV smaller total-energy values). The Hellmann - Feynman forces obtained within the DFT calculation are minimized via a geometry optimization in GADGET. Therefore, we search for a local mimimum on the potential energy surface.

Chapter 3

Theory II: A few concepts of many-body theory

The Kohn-Sham equation 2.11 is an effective one-particle equation. The one-particle approximation neglects many-body effects such as the correlated behaviour of electrons, and maps the many-body problem on Schrödinger-like one-particle equations such as Eq. 2.11 with an effective potential. This framework can't handle every interesting physical phenomenon.
Without any claim to be complete at this point, a few concepts of many-body theory are introduced in this chapter. A very intuitive guide through this exciting field was written by Richard D. Mattuck [19]. The following is based on Ref. [19].

3.1 Quasi particles

The quasi-particle concept and important concequences can be understood via a simple 'Gedanken' experiment: You may think of a box full of negative ions (-). Now consider a positive ion (+) that travels through the box (Figure 3.1). What happens is that the positive ion gets surrounded by some negative ones due to Coloumb interaction. The resulting particle (positive ion and

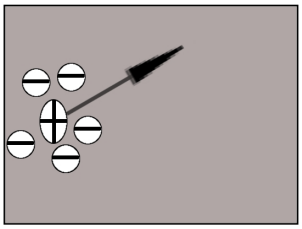

Figure 3.1: The quasi-particle picture - positive ion covered by negative ions

some covering negative ion) is now called a **quasi particle**. In quantum physics the quasi particle is also called the *coated* or *dressed* particle. Without its cloud the coated or dressed particle is called the *real* or *bare* particle. So we have:

$$\textit{real particle} + \textit{cloud} = \textit{coated particle} \tag{3.1}$$

or equivalently

$$\textit{bare particle} + \textit{clothing} = \textit{dressed particle}. \tag{3.2}$$

From this intuitive picture one can guess some basic properties of a quasi particle: First, if there are already other positive ions in the system and hence other positive ions coated by negative and vice versa negative ions coated by positive, the interaction between those 'shielded' quasi particles will be much weaker than between the unshielded bare particles (this is in fact the reason why the 'independent electron approximation' or 'Sommerfeld' model for metals is quite successful despite its crude assumption of independent particles: each electron pushes other electrons away and creates a surrounding shield - electrons in a metal are in fact nearly independent quasi particles). Second the quasi particle travelling through the system with $\boldsymbol{p}$ will still interact with other present quasi particles and thus keeps its momentum $\boldsymbol{p}$ only for an average time τ_p . So the quasi particle does travel through the system with momentum $\boldsymbol{p}$ for a time τ_p until it gets scattered. τ_p is called the *lifetime* and we can note:

$$\textit{Quasi particles have a lifetime } \tau_p. \tag{3.3}$$

This simple conclusion is of big importance as we know from elemantary quantum physics that non-interacting particles do have infinite lifetime.

3.2 Self-energy

Due to the cloud or clothes the particle does have to carry 'on its back', a new expression for the energy can be given:

$$\epsilon' = \frac{p^2}{2m^*}, \tag{3.4}$$

where m^* is called *effective mass* representing the cloud. ϵ' is the energy of the quasi particle and differs from the energy ϵ of the bare particle

$$\epsilon = \frac{p^2}{2m}. \tag{3.5}$$

The difference in energy of the quasi and the bare particle is called the *self-energy* of the quasi particle:

$$\epsilon_{\text{self}} = \epsilon_{\text{quasi}} - \epsilon_{\text{bare}}. \tag{3.6}$$

The term self-energy stems from the interpretation the particle enters the many-body system, creates a cloud of particles coating it, disturbing its motion and changing its energy. Thus, the self-energy is the energy corresponding to the particle interacting with itself via the many-body system.

3.3 The quantum mechanical propagator

The classical propagator is defined as the probability for propagation from point 1 to point 2. Due to the various (possible) processes along the path (*e.g.* the particle gets scattered) one can consider the propagation in several pieces and, in the classical case, sum them up to arrive at the total probability $P(2,1)$:

$$P(2,1) = P(\text{process I}) + P(\text{process II}) + ... \tag{3.7}$$

The fundamental difference in the quantum case is that the propagator $G(2,1)$ is now the sum of each processe's *probability amplitude*

$$G(2,1) = G(\text{process I}) + G(\text{process II}) + ... \tag{3.8}$$

and the total probability $P(2,1)$ yields:

$$P(2,1) = G^*G = |G(\text{I})|^2 + |G(\text{II})|^2 + G(\text{I})^*G(\text{II}) + G(\text{II})^*G(\text{I}) + ... \tag{3.9}$$

In the quantum case, the total probability is the sum of the probability of each process $|G(\text{i})|^2$ and of *interference terms*. A very plausible interpretation of those interference terms and how they govern the quantum world can be found in the first chapter of [20].
We now focus on the quantum mechanical propagator G and will see how the propagator looks like for the quasi particle. First we define the quantum mechanical propagator:

$$\begin{aligned} iG^+(k_2,k_1,t_2-t_1)_{t_2>t_1} = {} & \text{probability amplitude that, if at time} \\ & t_1 \text{ we add a particle in } \Phi_{k_1}(\boldsymbol{r}) \text{ to the} \\ & \text{interacting system in its ground state,} \\ & \text{the system will be inits ground state with} \\ & \text{an added particle in } \Phi_{k_2}(\boldsymbol{r}) \text{ at time } t_2. \end{aligned} \tag{3.10}$$

The $\Phi_k(\boldsymbol{r})$ are arbitrary single-particle eigenstates, the i is convention and the $+$ superscript tells us that $t_2 > t_1$. We also define:

$$iG^+(k_2,k_1,t_2-t_1)_{t_2\leq t_1} = 0. \tag{3.11}$$

We can choose the $\Phi_k(\boldsymbol{r})$ to be eigenstates of the unperturbed Hamiltonian H_0:

$$H_0 = \frac{-\nabla^2}{2m} + U(\boldsymbol{r}). \tag{3.12}$$

Then, if we set $U(\boldsymbol{r}) = 0$ (*i.e.* the free particle case), by the time-indipendent Schrödinger equation, we get:

$$\Phi_k(\boldsymbol{r}) = \frac{1}{\sqrt{\Omega}} e^{i\boldsymbol{k}\boldsymbol{r}}; \quad \epsilon_k = \frac{k^2}{2m}. \tag{3.13}$$

We can assume the wavefunction at time t_1 to be the wavefunction of the free particle to be $\Phi_{k_1}(\boldsymbol{r})$:

$$\psi(\boldsymbol{r}, t_1) = \Phi_{k_1}(\boldsymbol{r}). \tag{3.14}$$

If we let the wavefunction evolve, by the time t_2 we will find

$$\psi(\boldsymbol{r}, t_2) = \Phi_{k_1}(\boldsymbol{r}) e^{-i\epsilon_{k_1}(t_2 - t_1)}. \tag{3.15}$$

We can now calculate the propagator of the free particle G_0^+ (no interaction; also called *free propagator*), *i.e.* the probability amplitude for the particle being in state $\Phi_{k_2}(\boldsymbol{r})$ at time t_2:

$$\langle \Phi_{k_2} | \psi(t_2) \rangle = \int \mathrm{d}^3 r \ \Phi^*_{k_2}(\boldsymbol{r}) \psi(\boldsymbol{r}, t_2) = e^{-i\epsilon_{k_1}(t_2 - t_1)} \int \mathrm{d}^3 r \ \Phi^*_{k_2}(\boldsymbol{r}) \Phi_{k_1}(\boldsymbol{r}) =$$
$$= e^{-i\epsilon_{k_1}(t_2 - t_1)} \delta_{k_2, k_1}. \tag{3.16}$$

Applying Eq. 3.8 we arrive at the free propagator:

$$G_0^+(k_2, k_1, t_2 - t_1) = -i\Theta_{t_2 - t_1} e^{-i\epsilon_{k_1}(t_2 - t_1)} \delta_{k_2, k_1} = \delta_{k_2, k_1} G_0^+(k_1, t_2 - t_1), \tag{3.17}$$

or in general

$$G_0^+(k, t_2 - t_1) = -i\Theta_{t_2 - t_1} e^{-i\epsilon_k(t_2 - t_1)}. \tag{3.18}$$

Θ is the unit-step function and preserves Eq. 3.11. We perform the Fourier transform of the free propagator

$$G_0^+(k, \omega) = -i \int_{-\infty}^{\infty} \mathrm{d}(t_2 - t_1) \Theta_{t_2 - t_1} e^{i\omega(t_2 - t_1)} e^{-i\epsilon_k(t_2 - t_1)} = ... = \tag{3.19}$$
$$= \frac{1}{\omega - \epsilon_k} - \frac{e^{i(\omega - \epsilon_k)\ \infty}}{\omega - \epsilon_k}, \tag{3.20}$$

where divergence occurs at the upper limit of the integration intervall. In order to arrive at a sensible expression, we have to modify Eq. 3.18 and multiply the propagator by $e^{-\delta(t_2 - t_1)}$, where δ is an infinitesimal. Eq. 3.18 then becomes

$$G_0^+(k, t_2 - t_1) = -i\Theta_{t_2 - t_1} e^{-i(\epsilon_k - i\delta)(t_2 - t_1)}. \tag{3.21}$$

For finite $(t_2 - t_1)$, the modification does not have consequences because $(t_2 - t_1)\delta = 0$. For infinite $(t_2 - t_1)$ G_0^+ gets zero because $(t_2 - t_1)\delta = \infty \cdot \delta =$

∞. Thus the modification has no physical importance, since any physical observation is bound to a finite time. But the integral is not diverging any more and we can make use of Eq. 3.21:

$$G_0^+(k,\omega) = \frac{1}{\omega - \epsilon_k + i\delta} - \frac{e^{i(\omega-\epsilon_k+i\delta)\ \infty}}{\omega - \epsilon_k + i\delta} = \frac{1}{\omega - \epsilon_k + i\delta}. \tag{3.22}$$

From Eq. 3.22 we see that G_0^+ does have poles at (or to be more specific: infinitesimal close to) $\omega = \epsilon_k$, *i.e.* the energy of the added particle in state Φ_k. So the poles of the transformed propagator occur at values ω equal to the excited state energies minus the ground energy of the system!
We still want to find the quasi-particle propagator for an interacting system. In section 3.2 we saw that interacting particles behave like non-interacting particles, only a new energy ϵ' and a lifetime τ_k had to be introduced. Following this, we replace ϵ_k by ϵ'_k and multiply Eq. 3.18 with the factor $e^{-(t_2-t_1)/\tau_k}$ representing exponential decay and the lifetime. We also have to multiply by a factor $Z_k \leq 1$ to fullfil the Pauli principle for Fermi systems. We then get the quasi-particle propagator:

$$G^+_{quasi}(k, t_2 - t_1) = -iZ_k e^{-i\epsilon'_k(t_2-t_1)} e^{-(t_2-t_1)/\tau_k}. \tag{3.23}$$

We again perform the Fourier transform and arrive at

$$G^+_{quasi}(k,\omega) = \frac{Z_k}{\omega - \epsilon'_k + i\tau_k^{-1}}. \tag{3.24}$$

The exponential decay factor was responsible for vanishing the divergent behavior of the Fourier integral in Eq. 3.20.
As in the free particle case, the denominator in Eq. 3.24 determines the excited-state energies by

$$\omega_{pole} = \epsilon'_k - i\tau_k^{-1}, \tag{3.25}$$

whereas ϵ'_k is the real part and $i\tau_k^{-1}$ is the imaginary part of the complex energy ω_{pole}.

3.4 The Green's Function

To relate this more or less intuitive arguments of the last sections to fundamental quantum physics, the Green's function is introduced. A differential equation

$$\mathrm{L}\psi(\boldsymbol{x}, t) = f(\boldsymbol{x}, t), \tag{3.26}$$

has a associated **Green's function** G that obeys the following equation:

$$\mathrm{L}G(\boldsymbol{x} - \boldsymbol{x}', t - t') = \delta(\boldsymbol{x} - \boldsymbol{x}')\delta(t - t'). \tag{3.27}$$

The time-dependent Schrödinger equation for the free particle

$$\left(\frac{\nabla^2}{2m} + i\frac{\partial}{\partial t}\right)\psi(\boldsymbol{x}, t) = 0 \tag{3.28}$$

is a differential equation of the form 3.26 with $f(\boldsymbol{x}, t) = 0$. The Green's function associated to Eq. 3.28 thus obeys

$$\left(\frac{\nabla^2}{2m} + i\frac{\partial}{\partial t}\right)G(\boldsymbol{x} - \boldsymbol{x}', t - t') = \delta(\boldsymbol{x} - \boldsymbol{x}')\delta(t - t'). \tag{3.29}$$

By Fourier transforming G, we get

$$\left(-\frac{k^2}{2m} + i\frac{\partial}{\partial t}\right)G(\boldsymbol{k}, t - t') = \delta(t - t'). \tag{3.30}$$

For G we set the free propagator G_0^+ of Eq. 3.17

$$\begin{aligned}&\left(-\frac{k^2}{2m} + i\frac{\partial}{\partial t}\right)G_0^+(\boldsymbol{k}, t - t') = \\ &= \left(-\frac{k^2}{2m} + i\frac{\partial}{\partial t}\right)\left(-i\Theta_{t-t'}e^{-i\epsilon_k(t-t')}\delta(t - t')\right).\end{aligned} \tag{3.31}$$

By calculating the right side of 3.31, we find that Eq. 3.30 holds - the free propagator is the Green's function associated to the time-dependent Schrödinger equation for the free particle.

Chapter 4

Computational solid-state physics I: Modifying surface properties by adsorption of self-assembled monolayers

In this chapter the opportunity of modifying surface properties *via* the coverage by organic molecules arranged in a self-assembled pattern is discussed. In the first section the microscopic origin of monolayer induced interface modification is discussed by reviewing recent publications in this field. We afterwards sum up the methodology to then explore the influence of polar groups built into the backbone of organic monolayers.The latter was published by David A. Egger, Ferdinand Rissner, Gerold M. Rangger, Oliver T. Hofmann, Lukas Wittwer, Georg Heimel and Egbert Zojer in *Phys.Chem.Chem.Phys.* [3]. In the last section we discuss the electronic states of that monolayer in detail and explore methodological issues that were directly related to our findings.

4.1 The microscopic origin of SAM-induced interface modification and computational methodology

In the following section, concepts which are helpful in understanding the energetics of organic monolayers on surfaces are briefly reviewed. Furthermore, the computational methodology is introduced.

Naming convention: The molecules a self-assembled monolayer is build of are commonly seperated into three parts (see Fig. 4.1): The *head group*

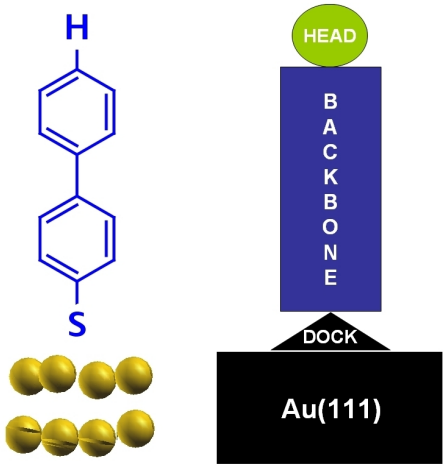

Figure 4.1: The naming convention: Backbone, head and docking group

pointing away from the surface (an H atom in the example in Fig. 4.1); the π-conjugated *backbone* (biphenyl in Fig. 4.1) and the *docking group* pointing towards the surface (an -S atom in Fig. 4.1).

Partitioning in the simulation: Following the arguments in Ref. [21] we choose the following calculation path to constitute the simulation of the monolayer-on-gold adsorption: (a) The geometry of the SAM on the gold surface is optimized, the two upper gold layers and the SAM atoms are allowed to relax (b) within this optimized geometry, the free-standing SAM (SAM without Au(111) surface) is saturated with hydrogen atoms; their position is optimized (c) the Au(111) surface within its optimized geometry (*i.e.* having the two upper layer reconstructed due to the SAM adsorption) and (d) the layer of hydrogen atoms the free-standing SAM was satured with. We thus perform calculations on the complete system, the saturated free-standing monolayer in its adsorption geometry, the Au(111) surface in its adsorption geometry and the layer of saturating hydrogen atoms.

The work function: The work function Φ of a metal is defined as the energy difference between the fermi level E_{F} and the vacuum level VL. As pointed out in Ref. [22], there are two types of vacuum levels: On the one hand, *the* vacuum level is the energy of a resting electron infinitely far away from any perturbation and is denoted as VL(∞). On the other hand, the vacuum level measured in experiment, hence the vacuum level of interest, is the energy of the electron right outside the solid, *i.e.* right at the surface. This vacuum level is denoted as VL(s). Due to the tailing of the electron cloud into the vacuum region and the so induced *interface dipole*, the electron right at the surface won't have the energy of the resting one far away from

any perturbations. Consequently VL(∞) and VL(s) are different. It is an experimental fact that the work function of a metal depends on which side of the crystal an electron is extracted from. Since the Fermi level is common, this is a consequence of different vacuum levels VL(s) resulting from different tailing of the electron cloud at different surfaces.

Consequently the electrostatics right at the surface are of great importance for the work function Φ. Adsorbing a polar monolayer will critically influence the work function. We will, therefore, first dicuss the electrostatic behavior of the free-standing monolayer.

Electrostatics of the free-standing monolayer: The left part of Fig. 4.1 shows a single polar molecule. This polar molecule has a dipole moment $\boldsymbol{d}$, as illustrated in Fig. 4.1. When a monolayer is formed of such polar molecules a dipole layer is built. [23, 24] In the example in Fig. 4.1, the resulting dipole moment is pointing in the $+z$-direction. Such a dipole layer induces a step in the electron potential energy

$$\Delta\phi = -\frac{1}{\epsilon_0} D(\boldsymbol{r}'), \tag{4.1}$$

where $D(\boldsymbol{r}')$ is the dipole area-density. As indicated in Fig. 4.1, this step happens *in* the SAM, the electron potential energy change is zero outside and constant inside the layer.

Electronic states of a self-assembled monolayer: The ionization potential IP is assumed to be the difference between the highest occupied molecular orbital HOMO and the vacuum level. The electron affinity EA is assumed to be the difference between the lowest unoccupied molecular orbital and the vacuum level. As explained, the vacuum level depends on interface dipoles. Consequently, the vacuum level is also affected when a dipole layer is present [21, 24]: There is a left side (*i.e.* docking side; see Fig. 4.1) vacuum level and a right side (*i.e.* head side; see Fig. 4.1) vacuum level. The change in the vacuum level is denoted as ΔE_{vac}

$$\Delta E_{\text{vac}} = \text{VL}_{\text{right}} - \text{VL}_{\text{left}} \tag{4.2}$$

and corresponds to Eq. 4.1. So the hypothetical, infinite monolayer splits space in two regions of different vacuum energy. As a consequence, each side of the monolayer has 'its own' IP (EA), called IP_{left} (EA_{left}) and IP_{right} (EA_{left}) as illustrated in Fig. 4.3.[21]:

Covalent bonding of the monolayer to the surface: The saturated monolayer is assumed to bond to the substrate upon hydrogen removal [2]. In order to extract the charge rearrangements induced by this bonding process,

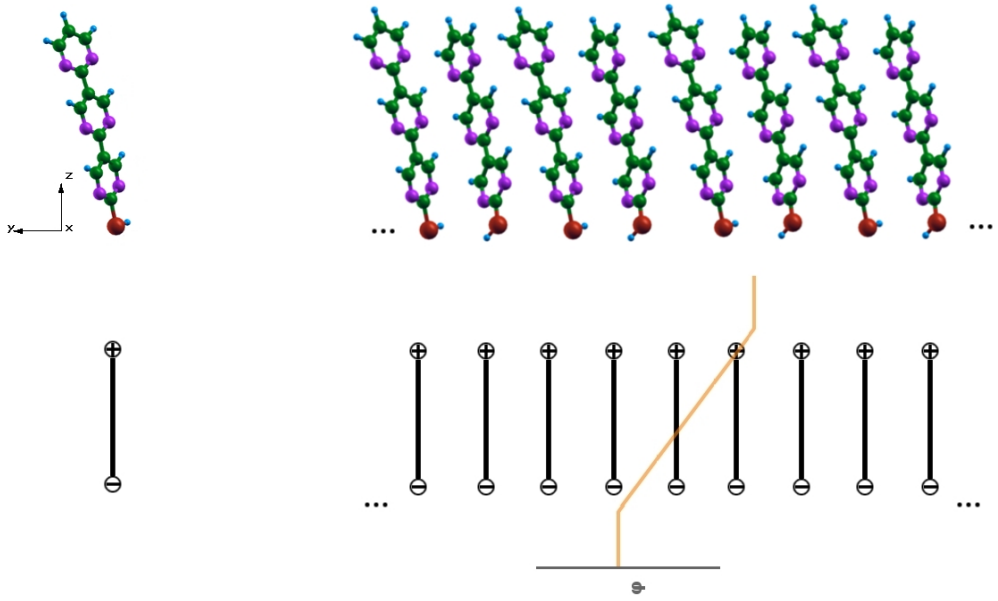

(a) (b)

Figure 4.2: (a) An isolated polar molecule and its dipole moment (b) Monolayer formed of polar molecules and the resulting dipole layer inducing a potential step

the following pathway is choosen [21, 24]: The charge density of the hydrogen atoms ρ_{H} is subtracted from the charge density of the saturated free-standing monolayer ρ_{sam}. The charge density of the Au(111) surface ρ_{Au} is added. The result is subtracted from the system's charge density ρ_{sys} and we get the bonding induced charge rearrangements ρ_{diff}:

$$\rho_{\mathrm{diff}} = \rho_{\mathrm{sys}} - (\rho_{\mathrm{sam}} - \rho_{\mathrm{H}} + \rho_{\mathrm{Au}}). \tag{4.3}$$

Those charge rearrangements arise from the Au-S bond formation and Pauli pushback [21]. In the top of Fig. 4.4 an exemplary plot of such charge rearrangements is shown. The distribution of the charge rearrangements clearly indicates an induced series of dipoles near the interface that rapidly decays both in the metal and the SAM [21, 24]. We can now integrate the one-dimensional Poisson's equation of electrostatics and get the bonding induced change in the electron potential energy, which is shown in the bottom of Fig. 4.4. As we see, those charge rearrangements have the same consequences as a dipole layer (see Fig. 4.1) - they shift the vacuum level [21]. The amplitude of that shift is often called *bond dipole* ΔE_{BD} [21, 24].

Modification of the work function: We can now summarize the consequences of monolayer adsorption on a metal surface [21, 24]: First, a mono-

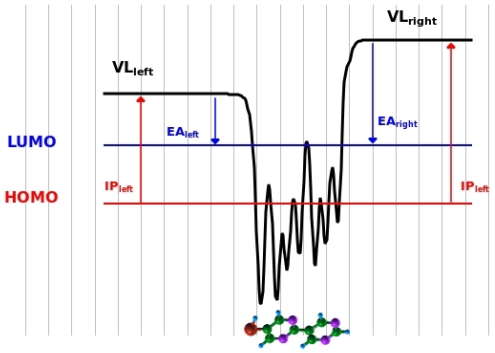

Figure 4.3: The isolated monolayer and each side's IP and EA

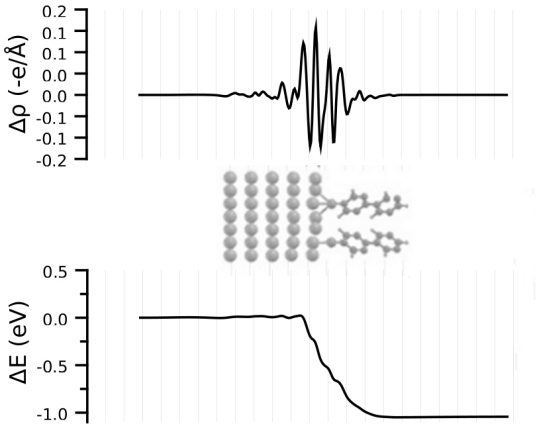

Figure 4.4: The charge rearrangements ρ_{diff} induced by the bonding from the SAM to the substrae (top) and the plane-integrated potential step with amplitude ΔE_{BD} (bottom) of a prototypical example

layer introduces a potential step of ΔE_{vac}. Second, the bonding of the SAM to the substrate induces another potential step of ΔE_{BD}, so the work-function modification $\Delta\Phi$ is

$$\Delta\Phi = \Delta E_{\text{vac}} + \Delta E_{\text{BD}}. \tag{4.4}$$

Those two contributions are usually independent of each other and can add up or partly compensate each other. $\Delta\Phi$ can be both positive and negative - SAM-adsorption provides a pathway to tune the work function Φ of a metal. The work-function modification $\Delta\Phi$ is demonstated in a summarizing plot in Fig. 4.5.

Level alignment: The relative alignment ΔE_{HOPS} between the Fermi energy of the system and the HOMO is another key parameter in device performance. The former HOMO in the unbonded SAM is called highest occupied

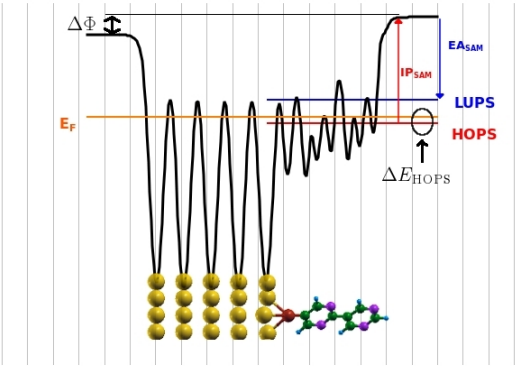

Figure 4.5: The complete system with the important observables $\Delta\Phi$ and ΔE_{HOPS} indicated

π state HOPS after the bonding process (the former LUMO becomes the LUPS). From the last paragraphs we see that it is not the molecular IP that governs ΔE_{HOPS} [21, 24], but the states in the SAM near the surface, *i.e.* IP_{left}. Starting from the difference between Φ_{Au} and IP_{left}, the HOMO is shifted by ΔE_{BD}. The difference between the energetic position of the HOPS and the Fermi energy E_{F} is called ΔE_{HOPS}. There is a small perturbation ($< 0.3\,\mathrm{eV}$) of the molecular states due to the bonding to the metal that is denoted as ΔE_{corr}. It is measured by the difference of the right side IP of the non-bonded monolayer IP_{right} and of the bonded monolayer IP_{sam}. We can now sum up those contributions to arrive at:

$$\Delta E_{\mathrm{HOPS}} = \Phi_{\mathrm{Au}} - IP_{\mathrm{left}} + \Delta E_{\mathrm{BD}} + \Delta E_{\mathrm{corr}}. \tag{4.5}$$

In Fig. 4.5 an overview of the final electronic states, the work-function modification $\Delta\Phi$ and the relative level alignment between the HOPS and E_{F} ΔE_{HOPS} is shown.

How to extract the quantities of interest: In this paragraph the extraction of the aforementioned quantities after the DFT calculation is listed:

- Work-function modification: $\Delta\Phi$ was calculated by using Eq. 4.4 and the z-component d_z of the dipole moment within the DFT calculation of the complete metal-organic system
- Level alignment: ΔE_{HOPS} was found by analyzing the density of states of the complete metal-organic system. The density of states was obtained using the script *obtainingdos* written by Gerold M. Rangger. There, we align the density of states at the metal Fermi-level. The metal Fermi-level can be found in the OUTCAR file produced by **VASP**.

The first pronounced peak below the metal Fermi energy was defined as the HOPS. Note that this method includes an artificial broadening of the density of states determined by the parameter σ in the VASP INCAR file.

- Vacuum levels: The vacuum levels were found by plane-averaging the electron potential energy of the free-standing SAM using the script *average* written by Gerold M. Rangger. The vacuum levels were found at the respective side of the monolayer induced potential modification, where the slope of the potential is equal to zero.

- SAM induced potential step: ΔE_{vac} was calculated by using Eq. 4.4 and the z-component d_z of the dipole moment within the DFT calculation of the isolated monolayer.

- Adsorption induced potential step: ΔE_{BD} was evaluated by subtracting the dipole moments of the metal, the isolated monolayer and the layer of hydrogen atoms from the complete system.

- Tilt angle of the long molecular axis: The tilt angle γ was calculated by extracting the components (x, y, z) of the vector connecting the carbon atom with the lowest and the carbon atom with the highest z-coordinate and using the octave script *tilt.m*:

```
function tilt(x,y,z)

tilt=acos(z*(1/sqrt(x^2+y^2+z^2)))*180/pi
end
```

Methodological summary: To simulate the surface we used the repeated slab approach, where 5 layers of gold atoms represented the gold surface and a vacuum gap of > 20 $\mathring{A}$ was introduced to prevent spurious electronic interactions between consecutive images of the slab in z-direction (see Fig. 4.1) The dimensions of the real-space unit cell were $5.11 \times 8.86 \times 45.28$ $\mathring{A}$. In that unit cell two molecules are arranged in the typical herringbone pattern (see Fig. 4.7). The fcc-hollow was initially chosen as the docking site in the starting geometry. A slight shift of the sulphur atoms towards the bridge site was observed in the optimized geometry. As start values for the tilt angle of the long molecular axis relative to the surface normal, we choose 11.1° and 12.4° for the bipyrimidine 'down' and 'up' (*vide infra*) conformations, respectively. Lukas Wittwer pre-optimized the geometric structure of the bipyrimidines. The mono- and terpyrimidine systems were optimized starting from the converged geometry of the respective bipyrimidine by removing or adding one pyrimidine ring. We performed DFT calculations (VASP 5.2 code) using a plane wave basis set (cutoff energy: 20.13 Ryd) and a PW91

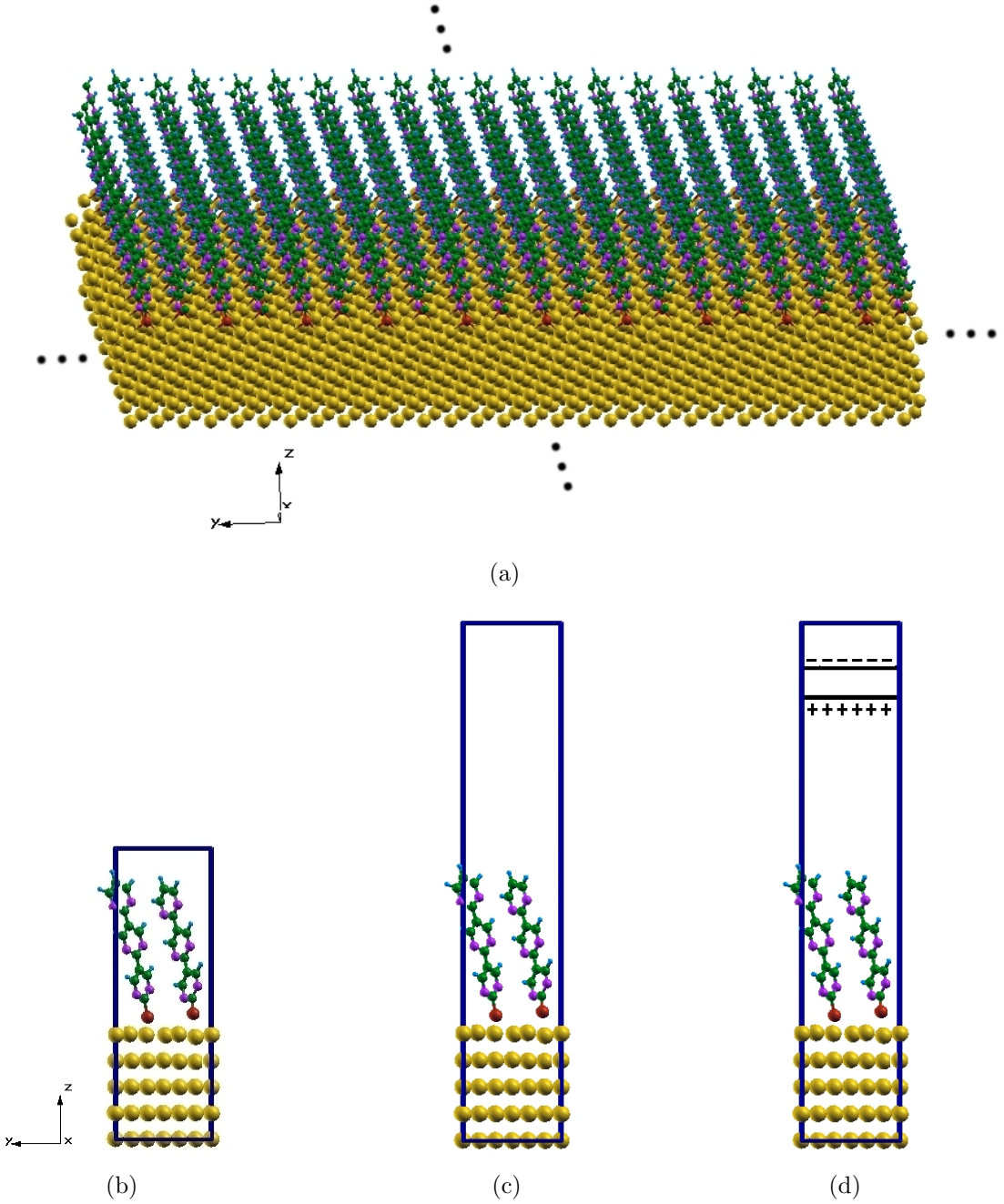

Figure 4.6: (a) Prototypical example of a monolayer assembled on the Au(111) surface: periodic in xy- and finite in z-direction (b) 'Intuitive' unit cell: the monolayer is followed by Au atoms with Au-interlayer distance (c) A vacuum gap is introduced to prevent unwanted interactions (d) Compensating electric fields by inserting a dipole sheet

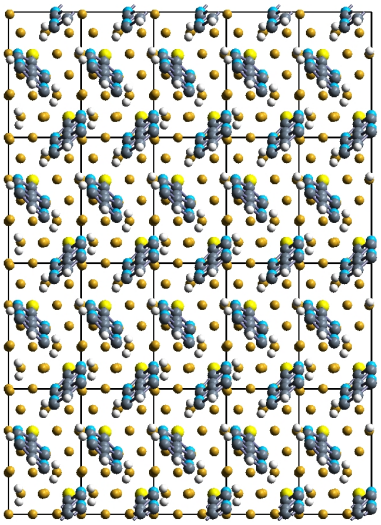

Figure 4.7: Top-view of the SAM in the typical herringbone pattern; the unit cell is indicated

exchange-correlation functional. The PW91 functional was chosen because it was found to perform slightly better for systems where van der Waals interaction is present [25] (compared to other semilocal functionals). An 8×5×1 Monkhorst-Pack grid of k-points was used to sample the reciprocal unit cell. Electronic ($\Delta E < 0.1$ meV) and dipole ($\Delta\mu < 0.003$ e$\mathring{A}$) convergence were tested carefully. To optimize the geometry, all atoms of the monolayer and the top two gold layers were relaxed until the maximum force component was < 0.01 eV/$\mathring{A}$. We employed the external tool GADGET to perform the geometry optimization in internal coordinates.

4.2 Distributing the dipoles

[1]In organic electronic devices, the alignment of the electrodes' Fermi-level relative to the frontier orbitals of the adjacent organic semiconductors critically influences device performance.[26] The most important parameter in this context is the electrode work function, Φ.One approach to adjust Φ is the adsorption of self-assembled monolayers (SAMs) of dipolar molecules.[27, 28, 29, 30, 31, 32] In-depth quantum-mechanical studies on the effect of various molecules have led to a microscopic understanding of the processes governing the electronic structure of the metal/SAM interface.[33, 34, 24, 35].
So far, the focus has been largely on the effect of end-group substituents, *e.g.*, dipolar donor- or acceptor-groups[29, 24, 23] or fluorinated segments

[1]The following contens were published in [3].

[27, 28, 29, 30] attached to a non-polar backbone. Here, we propose a novel approach: distributing a series of dipoles along the molecular backbone. This provides an additional 'chemical' handle for tuning interfacial properties, especially when adapting the number of polar repeat units in each molecule. Furthermore, it should modify the interaction between the SAM-forming molecules, and differences in the electric field distribution within the SAM can be expected to affect parameters like charge transport through the layer. The quantities of interest in the present computational study are the work-function modification, $\Delta\Phi$, due to the SAM and the alignment,ΔE_{HOPS}, between the Fermi level of the system and the HOMO-derived π-states (the HOPS) of the SAM. Specifically, we show that the distributed-dipole approach results in modifications of the interface energetics that differ significantly from those in conventional SAMs. This is especially true as far as the evolution of the aforementioned physical quantities of interest with the length of the backbone is concerned.

The calculations rely on density-functional theory (DFT) within the repeated-slab approach, applying the PW91 exchange-correlation functional and using the VASP code [36]. Geometry relaxations were performed in internal coordinates using the optimizer GADGET [18], three-dimensional representations of the systems were generated with XCrysDen. [37] The applied methodology follows Ref. [38] and is presented in 4.1.

We investigated thiols adsorbed on the Au(111) surface (Fig. 4.8 a) in a p($\sqrt{3} \times \sqrt{3}$) surface forming a herringbone pattern in analogy to what was found experimentally for biphenylthiols [39]. This procedure also ensures comparability with our previous calculations. [24, 23, 38] We chose (mono,] bi, and ter) pyrimidines as backbones, with the dipolar pyrimidine moieties linked in a head-to-tail fashion. Here, one has to distinguish between two possible orientations of the nitrogens relative to the docking group (and, thus, in the SAM relative to the metal substrate), referred to as 'N-up' (thiol group in 5-position) and 'N-down' (thiol group in 2-position), as shown in Fig. 4.8 b. In this way, the resulting molecular dipole moment points either towards ('N-up') or away from the metal surface ('N-down'). As reference systems with non-polar backbones we chose oligophenylthiols [24, 23, 38] (considering 1, 2, and 3 rings) bearing donor or acceptor head groups (Fig. 4.8 b). From the large pool of possible substituents, we chose the donor amine (-NH_2) and the acceptor trifluoromethyl (-CF_3) substituent as the resulting SAMs for two-ring backbones (the intermediate length case amongst the ones considered here) give rise to work-function modifications similar to the 'N-down' and 'N-up' bipyrimidines.

Conceptually, changing an electrode's work function by means of dipolar molecules results from two different microscopic origins: [23] First, the molecular dipole moments give rise to a step in the electrostatic potential energy across the (non-bonded) monolayer, referred to as ΔE_{vac}. As it is propor-

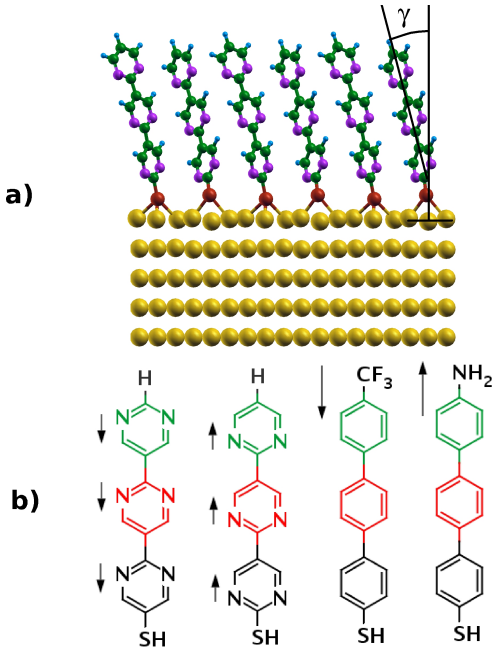

Figure 4.8: (a) Schematic representation of 'N-down' terpyrimidinethiol SAM adsorbed on Au(111). The tilt angle γ of the molecule relative to the surface normal is indicated. (b) Chemical structures of the four investigated molecules (from left to right): 'N-up' oligopyrimidinethiol (-SH attached at the 5 position); 'N-down' oligopyrimidinthiol (-SH attached at the 2 position); CF_3-substituted oligophenylthiol and NH_2-substituted oligophenylthiol. For each system 1, 2, and 3 rings were considered. The arrows schematically indicate the relevant molecular dipole moments.

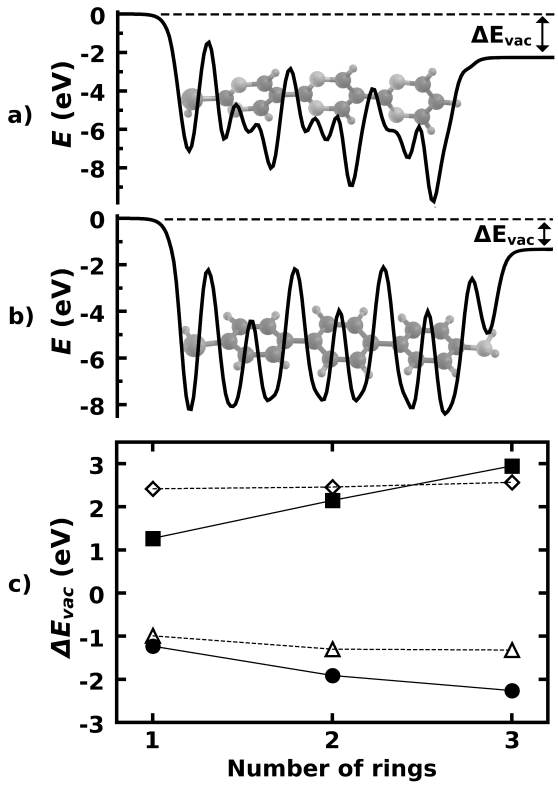

Figure 4.9: Plane-averaged electron potential energy of (a) 'N-down' terpyrimidinethiol and (b) NH_2-substituted terphenylthiol. The left vacuum energy is chosen as the energy reference (c) Backbone length dependence of $\Delta E_{\mathrm{vac}}$for 'N-up' oligopyrimidinthiol (filled squares), 'N-down' oligopyrimidinthiol (filled circles), CF_3-substituted (open diamonds), and NH_2-substituted terphenylthiol (open triangles).

tional to the component of the dipoles perpendicular to the substrate surface, the molecular orientation plays a decisive role. [40] Furthermore, electrostatic interactions between the molecules forming the monolayer induce coverage-dependent depolarization effects, [34, 41] ypically resulting in a sub-linear increase of the magnitude of $\Delta E_{\mathrm{vac}}$with the packing density. [42] Second, an additional shift in the potential energy (with amplitude ΔE_{BD}) is caused by interfacial charge rearrangements upon Au-SAM bond formation. To sum up, $\Delta\Phi = \Delta E_{\mathrm{vac}} + \Delta E_{\mathrm{BD}}$. We first analyze the electrostatics of the isolated monolayers (with the sulphur atoms saturated by hydrogens). Figs. 4.9 a and 4.9 b show the plane-averaged electron potential energy across 'N-down' terpyrimidinethiol and NH_2-substitued terphenylthiol. For the non-polar backbone, all rings are at virtually the same potential; the potential drop responsible for $\Delta E_{\mathrm{vac}}$is confined to the region of the NH_2 substituent. In contrast, for 'N-down' terpyrimidinethiol, a continuous decrease of the

potential across the entire backbone is found, as each polar ring introduces a step in the potential energy landscape. When comparing the 'N-up' conformations with the CF_3-substituted oligophenylthiol SAMs, an analogous situation with different sign of $\Delta E_{\mathrm{vac}}$is observed (not plotted). The total potential step across the monolayer, ΔE_{vac}, is plotted in Fig. 4.9c as a function of the number of pyrimidine/phenyl rings.[2]

As expected, [41] this potential energy step changes only slightly with the length of the backbone in the head-group substituted reference systems. In fact, also previous studies [43, 44] have found a small variation of the work function with the length of the adsorbed molecules in SAMs of (fluorinated) alkylthiolates, which could be largely attributed to changes in the geometry of the alkyl backbone. [44] The (minor) length dependence of ΔE_{vac}in the case of the -NH_2 substituent is in part due to a slight increase of the molecular dipole moment, similar to what has been observed for nitro-substituted phenylenevinylene [41]. The main origin, however, is purely geometric: The tilt angle Γ ((Fig. 4.8 a) of the NH_2-substituted phenylthiols decreases with chain length (Table 4.1), which results in an increase of the component of the dipole moment perpendicular to the surface. Importantly, a pronounced dependence on the backbone length is found for the oligopyrimidinethiols, where every additional ring significantly contributes to a further change in the potential energy. Moreover a close to linear evolution is observed. While this is what one might have expected for molecules resembling a linear series of dipoles, it is actually far from trivial as (i) the intra-molecular interaction between the rings changes upon elongating the backbone[3] (ii) the inter-molecular interactions (including depolarization) can be expected to change with chain length and (iii) significant changes of the backbone orientation (and thus of the component of the dipole moment perpendicular to the surface) are found with increasing length of the backbone, *i.e.*, the tilt angle γ decreases with increasing number of repeat units (see Table 4.1). The second contribution to the SAM-induced work-function modification, ΔE_{BD}, is obtained by analyzing the adsorption under the assumption of hydrogen

[2]H-saturation of the thiol group introduces another dipole moment, affecting also the resulting ΔE_{vac}. While the C-S-H bond angle is unambiguous the C-C-S-H dihedral angle is not. Although the position of the saturating hydrogen atoms was chosen in a consistent way for all systems, geometrical differences (such as significantly different molecular tilt angles or the orientation of the axis around which the molecules are actually tilted) result in a different effect of the S-H bond on ΔE_{vac}. However, we stress that ΔE_{vac} is not an experimentally accessible quantity (*i.e.*, there is no 'correct' way of determining it), as it characterizes the hypothetical free-standing monolayers. The dependence of ΔE_{vac} on the H positions is fully compensated by ΔE_{BD}, thus keeping$\Delta\Phi$ and ΔE_{HOPS}, of course, independent of the H-position in the saturated monolayer.

[3]The three rings are not equivalent. The first carries a thiol group, the centre ring is coupled to two adjacent pyrimidine units, and the third (hydrogen-terminated) ring is coupled to only one pyrimidine unit; a certain amount of charge transfer between these three distinct moieties cannot be excluded a priori.

Table 4.1: DFT-calculated work-function modification, $\Delta\Phi$, magnitude of the induced potential energy shift due to the bond dipole, ΔE_{BD}, potential step across the saturated monolayer, ΔE_{vac}, difference between EF of the system and the HOPS of the SAM, ΔE_{HOPS}, and tilt angle, γ, of the long molecular axes relative to the surface normal; as there are two inequivalent molecules in the unit cell, average values are reported for γ.

SAM	rings	$\Delta\Phi(eV)$	$\Delta E_{\mathrm{BD}}(eV)$	$\Delta E_{\mathrm{vac}}(eV)$	$\Delta E_{\mathrm{HOPS}}(eV)$	$\gamma(^\circ)$
'N-up'	1	0.35	-0.94	1.27	-0.91	37.2
	2	1.09	-1.07	2.15	-0.17	26.7
	3	**0.98**	**-1.99**	2.94	**-0.15**	19.1
'N-down'	1	-1.96	-0.74	-1.23	-1.67	31.5
	2	-2.58	-0.68	-1.91	-1.44	26.7
	3	-3.11	-0.85	-2.26	-1.37	24.0
'CF_3'	1	1.34	-1.08	2.42	-1.06	16.2
	2	1.33	-1.13	2.46	-1.01	13.7
	3	1.39	-1.18	2.57	-0.97	12.2
'NH_2'	1	-2.21	-1.23	-0.99	-0.83	25.2
	2	-2.48[a]	-1.18[a]	-1.30[a]	-0.86[a]	17.1
	3	-2.49	-1.17	-1.32	-0.86	15.7

[a] These values differ slightly from those reported in Ref. [24] due to a different geometry-optimization scheme used for the present work.

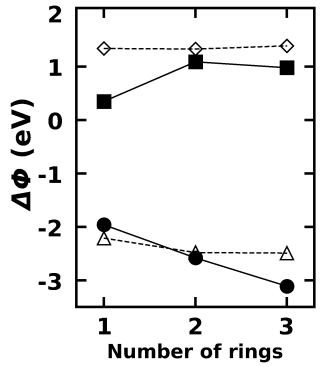

Figure 4.10: Backbone length dependence of the work-function modification $\Delta\Phi$ for 'N-up' oligopyrimidinethiol (filled squares), 'N-down' oligopyrimidinethiol (filled circles), CF_3-substituted (open diamonds) and NH_2-substituted terphenylenethiol (open triangles).

removal and Au-S bond formation. Table 4.1 lists the values for all twelve systems. ΔE_{BD} primarily depends on the docking chemistry. Accordingly, a similar value of ΔE_{BD} is found for all phenylthiol-docked SAMs independent of the end-group substituent, as the latter does not affect the docking group side of the SAM (cf., Table 4.1). For the 'N-down' pyrimidinethiol SAMs, ΔE_{BD} is somewhat decreased compared to the biphenylthiols, and its magnitude is almost independent of the number of repeat units. Consequently, the evolution of ΔE_{vac} from Fig. 4.9c is translated into an almost linear dependence of the work-function modification on the number of 'N-down' oriented pyrimidines as shown in Fig. 4.10. This indicates that distributing dipoles throughout the molecular entity indeed provides a strategy to tune the work-function modification over a wide range in a systematic way. One might even be tempted to think that arbitrarily large work-function changes could be realized as long as one merely synthesized a long-enough backbone (provided that such molecules would actually form closely packed SAMs). That assessment, however, is put into perspective by the results for the pyrimidine 'N-up' configuration (cf., Fig. 4.10). There, no linear evolution of ΔE_{vac} with the number of repeat units is observed. It rather saturates at two rings and never exceeds the value for the CF_3-substituted biphenylthiol (actually, for three rings even a slight decrease is observed). From Table 4.1, it becomes obvious that the saturation of $\Delta\Phi$for the 3-ring pyrimidine 'N-up' SAM is the consequence of the exceedingly large ΔE_{BD} in that system.
In order to understand the ΔE_{BD} value of the 'N-up' terpyrimidine it is necessary to consider the energetic alignment between the molecular states and the Fermi-level of the system. As shown in Table 4.1, ΔE_{HOPS} (defined as the energy difference between the HOPS peak and E_F) amounts to -0.91eV in

'N-up' monopyrimidine. Upon elongating the backbone, the HOMO-LUMO gap decreases, as does the ionisation potential of the SAM at the side of the docking group; together with ΔE_{BD}, the latter determines the level alignment. [24, 23] Consequently, also ΔE_{HOPS} becomes smaller and reaches a value of -0.17eV. If that trend continued for terpyrimidine, its HOPS would come to lie above the Fermi level, which would be inconsistent with a population of the electronic states according to the Fermi-Dirac statistics. Instead, as soon as the tail of the HOPS-related density of states crosses $\mathrm{E_F}$, electrons are redistributed within SAM and metal, resulting in a sizeable extra interfacial dipole layer. This essentially pins the HOPS of the SAM at $\mathrm{E_F}$, as can be inferred from the fact that ΔE_{HOPS} in terpyrimidinethiol is only slightly smaller than in bipyrimidinethiol. The pinning-induced interface dipole then manifests itself in the very large ΔE_{BD} for the terpyrimidine SAM in the 'N-up' configuration. In fact, a closer look at the ΔE_{BD} values in Table 4.1 indicates that already in the two-ring system, weak Fermi-level pinning is at work. An important conclusion from this finding is that there is a natural limit for the maximum achievable $\Delta\Phi$ within the distributed-dipole approach, which is determined by the energies of the frontier electronic states in the SAM. That is, $\Delta\Phi$ can be increased by elongating the molecular backbone only as long as Fermi-level pinning can be avoided.

As for the work-function modification and ΔE_{vac}, a qualitatively different behaviour is observed also for the level alignment in the 'N-down' systems: Already for the one-ring system, the absolute value of ΔE_{HOPS} is by 0.76 eV larger than for the corresponding 'N-up' structure. This is insofar remarkable, as one is dealing with an identical molecular backbone that is merely attached in a different orientation to the sulphur docking groups bonded to the metal. The difference in ΔE_{HOPS} between the 'N-up' and 'N-down' configurations further increases for bipyrimidinethiol, where it reaches the maximum value of 1.27 eV. This behaviour is in sharp contrast to what is seen in the two reference systems, $\mathrm{CF_3}$- and $\mathrm{NH_2}$-substituted biphenylthiol. In spite of the fact that they yield work-function modifications equivalent to the 'N-up' and 'N-down' bipyrimidinethiol SAMs, the differences between their ΔE_{HOPS} are very minor, as observed in all end-group substituted systems studied so far. [24, 40] The reason for these qualitatively different trends is rooted in the fact that, in the absence of Fermi-level pinning, the level alignment is determined by the ionisation potential of the (non-bonded) SAM on that side of the layer, which is eventually docked to the metal. This quantity is virtually unaffected by the dipoles induced by end-group substituents which, naturally, are attached to the opposite side of the SAM. [23] It is, however, of course modified by dipoles distributed within the backbone and by dipoles close to or at the docking group.

In summary, we discussed a novel approach to tuning the interface energetics of metal/SAM systems through distributed dipoles built into the molecular

backbones; in the presented prototypical case, this is realized by pyrimidine rings linked in para position. The direction of the SAM-induced work-function change can be controlled by the pyrimidine orientation and its magnitude increases linearly with the number of repeat units (as long as one can avoid Fermi-level pinning). This is in sharp contrast to what is known from SAMs in which the work-function is changed by polar end-group substituents on otherwise non-polar backbones. Unlike in these systems, one finds that, for the oligopyrimidine-based SAMs, different work-function modifications go hand in hand with differences in the alignment between the molecular states and the Fermi-level. In fact, we observe differences in the level alignment of up to 1.27 eV for chemically equivalent backbones docked to the substrate in different orientations.

4.3 Collective effects in self-assembled monolayers with distributed dipole moments

Self-assembled monolayers (SAMs) are promising candidates in nanotechnology. Their ability to modify macroscopic electronic properties of metal surfaces makes them especially attractive for organic (opto-)electronics. However, the understanding of processes governing the physics of those supramolecular structures is essential and not yet complete. To anticipate the physical properties of a SAM from the properties of the molecules it contains was shown to be insufficient [21, 45].
In this section the electronic structure of oligopyrimidine monolayers is investigated. Those molecules have interesting properties due to dipoles distributed along the backbone [3]. A pronounced change in the Kohn-Sham gap [46] as a function of the packing density for monolayers formed of those molecules is found. We explain those findings by collective electrostatic effects.

4.3.1 Introduction and structure of the system

We investigated monolayers formed of oligopyrimidine molecules (see Fig. 4.11). Here, one has the possibility to choose between two different orientations of the nitrogens relative to the docking group, previously referred to as 'N-up' (thiol group in 5-position) and 'N-down' (thiol group in 2-position), as shown in Fig. 4.11. In this way, the resulting molecular dipole moment points either towards ('N-up') or away from the metal surface ('N-down'). We choose 'N-up' terpyrimidinethiol to investigate the electronic structure of a monolayer built of polar building blocks. The electronic states within the 'N-up' oligopyrimidine monolayers were found to shift when elongating the backbone [3]. Futhermore, the molecular dipole moment of 'N-up' ter-

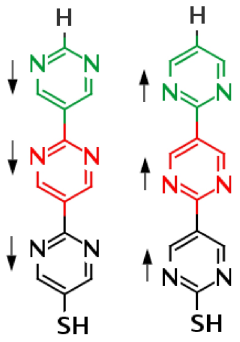

Figure 4.11: The two possible confirmations of terpyrimidinethiol ('N-up' and 'N-down') with their relevant dipole moments schematically indicated

pyrimidinethiol is the largest one of the investigated systems in Ref. [3]. For this SAM, we focused on the density of states within the layer as a function of the packing density. In this way, the transition from the properties of the isolated molecule (*i.e.* the low coverage regime) to that of the closely packed monolayer can be observed.

To perform the coverage dependent calculations, we removed one molecule from our p($\sqrt{3} \times \sqrt{3}$) surface unit-cell yielding a coverage of $\Theta = \frac{1}{2}$. We subsequently doubled the dimension of the unit-cell in the xy-plane and accordingly reduced the number of k-points to obtain coverages from $\Theta = \frac{1}{4}$ down to $\Theta = \frac{1}{64}$, which approximates the isolated molecule [42]. The free-standing SAM was obtained by optimizing the geometry of the densely packed monolayer on five layers of Au(111). Monolayers of smaller coverages were not optimized concerning the geometric structure. As we focused on electrostatic influence on the electronic structure, we tried to prevent geometric effects.

4.3.2 Results and discussion - coverage dependent density of states

To understand the influence of distributed dipoles on the electronic structure of a SAM, we varied the coverage of the free-standing 'N-up' terpyrimidinethiol monolayer. This procedure is known to crucially affect the electrostatics and eigenstates of a monolayer [45, 42, 34]. For example, in Ref. [42] the highest occupied molecular orbital HOMO of head-group substituted biphenylthiols was found to shift about 0.5 eV when going from low to full coverage. Here, it would be interesting to know how the Kohn-Sham gap reacts to a change of the packing density.

The black solid line in Fig. 4.12 shows the coverage dependent density of states of 'N-up' terpyrimidinethiol aligned to the docking side vacuum level.

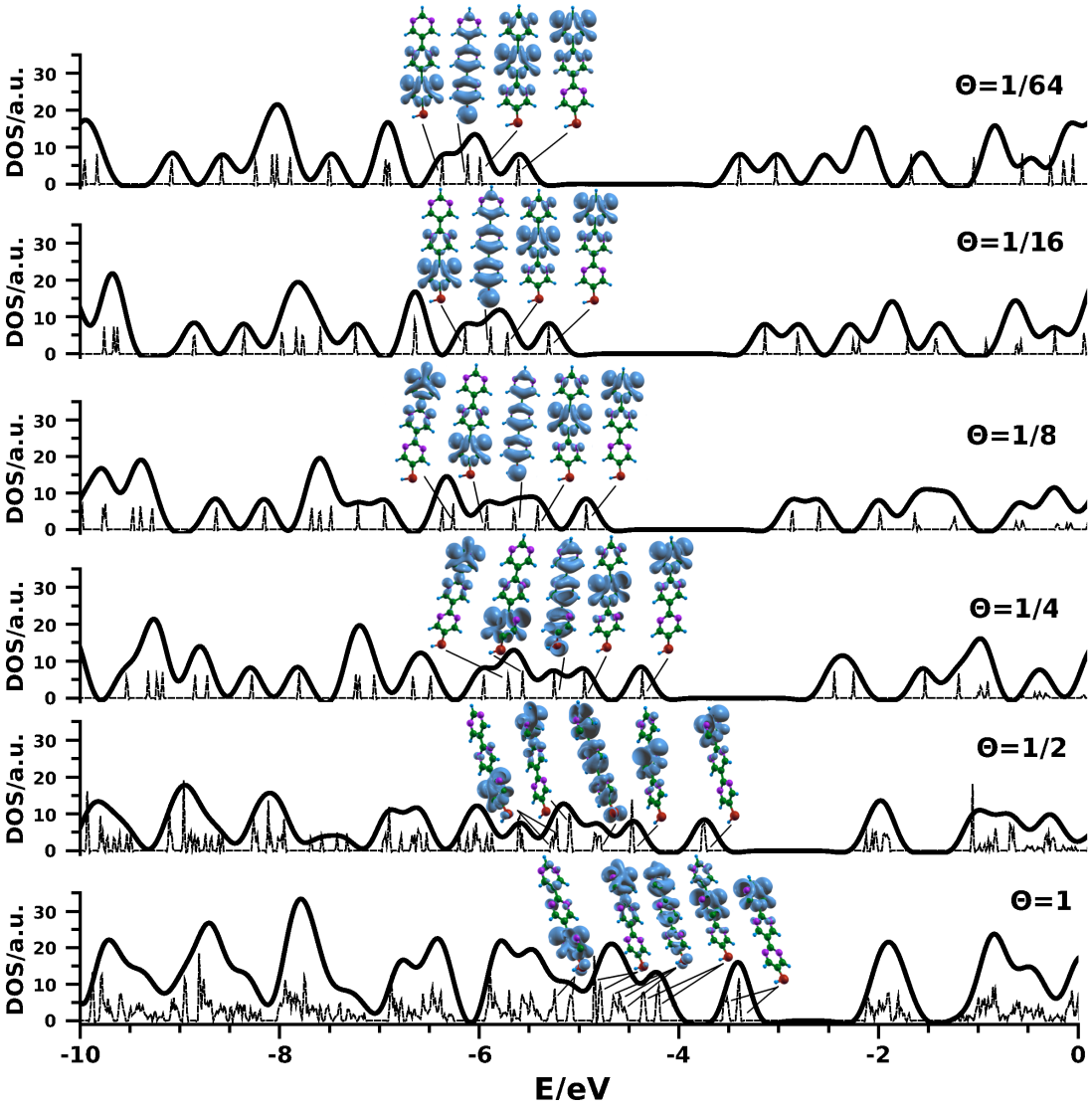

Figure 4.12: Density of states of the free-standing 'N-up' terpyrimidinethiol monolayer aligned at the docking-side vacuum level for different coverages. The dashed lines indicate the density of states corresponding to the less broadened density of states, the associated LDOS is illustrated

The docking side vacuum level was choosen as a reference due to the importance of the alignment between the metal Fermi-level and electronic states in the adsorbed SAM [21, 24]. It is found that, when increasing the coverage, the density of states changes drastically: We find the HOMO shifting by more than 1 eV when going from the isolated molecule to the densely packed SAM. The Kohn-Sham gap, defined as the energy difference between the HOMO and the LUMO, is decreased by 0.7 eV from 2.2 eV to 1.5 eV when increasing the packing density. The LDOS of the unoccupied states was not calculated up to now. It would also be interesting to know how the π-π^* gap changes when increasing the packing density.

In order to understand this remarkable result, the shape and position of those shifting orbitals are investigated. We reduced the broadening of the density of states to find the discrete eigenstates in the spectrum[4]. The thin dashed line in Fig. 4.12 shows the less broadened density of states. We find that, at a coverage of $\Theta = \frac{1}{2}$, the eigenstates start to disperse. Furthermore, when going to the full-coverage regime, one finds even more peaks very close in energy in the narrow density of states. This is due to the presence of the second inequivalent molecule at $\Theta = 1$ (*vide supra*). We choose not to distinguish between states derived from each of the two molecules in the unit-cell and therefore have several peaks associated to one orbital in the high-coverage regime. At $\Theta = \frac{1}{64}$ one finds unoccupied states vanishing in the less broadened DOS. From experience, this can be the case when reading in a charge density at the beginning of the DFT calculation.

The local density of states was then obtained by integrating around the peaks of the less broadened density of states. We continually adjusted the integration interval until the number of bands in the *.out* file of the calculation was either one or two (in the full-coverage regime two molecules are present in the unit-cell). Therefore we resolved one molecular orbital in each case. The LDOS of 'N-up' terpyrimidinethiol corresponding to the assigned peaks in the less broadened density of states is shown in Fig. 4.12. Starting at a coverage of $\theta = \frac{1}{64}$ we find the two highest occupied states to have σ-character (see Fig. 4.12). Moreover, a pronounced localization of those molecular orbitals is found. The HOMO is confined to the two uppermost (relative to the thiol docking-group) pyrimidine rings where the topmost ring carries the most part of the electron density. For the second highest occupied state, the HOMO-1, we find the same orbital with the only difference being the bigger part of the orbital located at the middle ring. The HOMO-2 is a π-state delocalized over the whole molecule, whereas the HOMO-3 completes the series of localized σ-orbitals with the major part of electron density on the docking-side ring. If following the orbitals from $\theta = \frac{1}{8}$ to full coverage, the former HOMO-4 shifts up in energy and becomes the HOMO-3 at half

[4] A Methfessel-Paxton [47] occupation scheme was employed. We reduced the broadening from $\sigma = 0.2$ to $\sigma = 0.01$

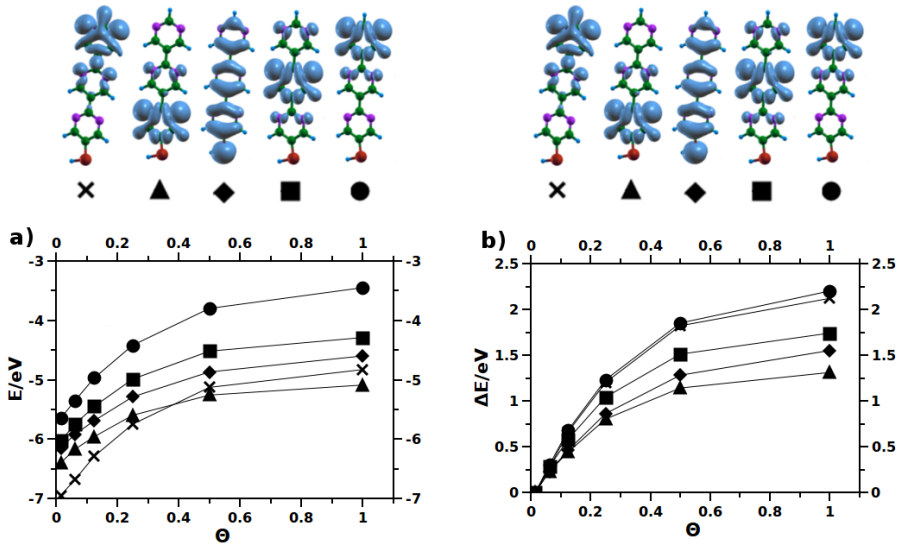

Figure 4.13: Absolute (a) and relative (b) energy difference of the different orbitals depending on the coverage. In (b) the energy position of each orbital at $\theta = \frac{1}{64}$ was set to zero

coverage.

Fig. 4.13 illustrates each orbital's evolution when increasing the coverage. In Fig. 4.13a) the absolute position in energy of the respective states aligned to the docking-side vacuum level is shown. As expected [42], a sublinear dependence on the coverage for the energy positions of all orbitals is found for the 'N-up'-terpyrimidinethiol monolayer. The orbital assigned as the HOMO-4 in the low-coverage regime 'passes by' the former HOMO-3 at half coverage, as already seen in Fig. 4.12. The energy difference relative to each orbital's energy position at $\Theta = \frac{1}{64}$ is illustrated in Fig. 4.13b). Different evolutions for the respective orbitals are found when increasing the coverage. Obviously the shifting of the orbitals depends on their spatial distribution in the monolayer: Orbitals localized at the head-group oriented ring of the SAM shift strongly in energy while orbitals localized in the lower part of the molecule, as well as the delocalized π-state, shift less. Interestingly, we find the HOMO and the primal HOMO-4, despite of being seperated by more than 1 eV in energy, to shift *equally* when increasing the coverage.

Those findinds are rationalized by inherent modifications of the electrostatic situation when changing the packing density. Fig. 4.14 shows the plane-averaged electron potential energy aligned at the docking-side vacuum level for two different coverages $\Theta = 1$ and $\Theta = \frac{1}{4}$. The induced potential step is a function of the packing density. Furthermore, a continuous decrease of the potential across the entire backbone is found for both coverages. A continuous modification of the potential landscape along the long-molecular

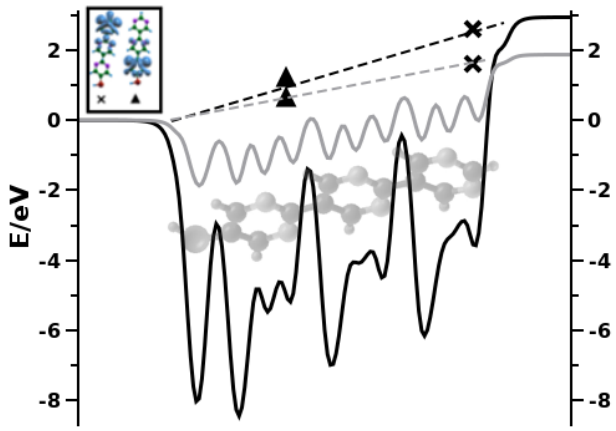

Figure 4.14: Plane-averaged electron potential energy aligned at the docking-side vacuum level for $\Theta = 1$ (black solid line) and $\Theta = \frac{1}{4}$ (grey solid line). The black dashed line and grey dashed line serve as a guide to the reader's eye and illustrate the slope of the potential in the respective coverages. The symbols depict the consequence of orbitals located at different ends of the monolayer

axis in the high-coverage regime was already shown to be a consequence of distributing dipoles [3]. From electrostatic considerations one finds a constant change of the electrostatic potential along such dipole layers. Consequently, the slope of the potential along the backbone is a function of the packing density as indicated by the dashed lines in Fig. 4.14. The symbols in Fig. 4.14 illustrate the consequence of states localized at different ends of the monolayer. From this picture it makes perfect sense that the shift of the orbitals depends on there position in the SAM: Orbitals located at the head-group oriented tail will certainly shift more when increasing the packing density than states located near the docking-side ring or delocalized orbitals. The ensemble of molecules present in a densely packed SAM leads to an entire new electrostatic situation resulting in a fundamental change of the eigenvalue spectrum.

To understand the reduction of the Kohn-Sham gap, we projected the density of states on each layer of rings in the SAM. Fig. 4.15 shows this so called RDOS aligned at the docking-side vacuum level as a function of the coverage. We find our aforementioned conclusions confirmed in the RDOS: The shifting of the states when going to a higher coverage increases towards the head-group oriented ring. Comparing the HOMO and HOMO-1 at $\Theta = \frac{1}{64}$ and $\Theta = 1$, we find their energetic difference increasing from 0.38 eV in the isolated molecule to 0.82 eV at full coverage. At $\Theta = \frac{1}{64}$, the LUMO is distributed over all three rings. By increasing the coverage, we find the delocalized LUMO to shift in energy. The LUMO+1 is localized at the docking-side oriented ring at low coverage. Therefore, the LUMO+1 shifts less than the delocalized LUMO. Indeed, we find the main portion of the LUMO to be on the docking-side ring at $\Theta = 1$. Occupied and unoccupied states localized at each end of the monolayer are the origin of the Kohn-Sham gap reduction when increasing the coverage.

Compared to previous work in our group, it was unexpected to find the HOMO with σ character. At least at $\Theta = \frac{1}{64}$, which was assumed to be the isolated molecule, a π-HOMO would have been expected. In fact, $\Theta = \frac{1}{64}$ is not the isolated molecule, but the molecule in a very large unit-cell. From our findings and the long-range Coloumb interaction we concluded that spurious electric fiels might be responsbible for a shifting of the σ-states which otherwise would be down in energy at a coverage of $\Theta = \frac{1}{64}$.

4.3.3 Calculations on the isolated 'N-up' molecule - functional dependent electronic structure

To test if a coverage of $\Theta = \frac{1}{64}$ fits the situation of an isolated molecule, we performed calculations on the 'N-up' terpyrimidinethiol molecule in GAUSSIAN03[48]. The molecule was investigated in its geometric structure of the monolayer to rule out geometric effects. We applied a series of aug-

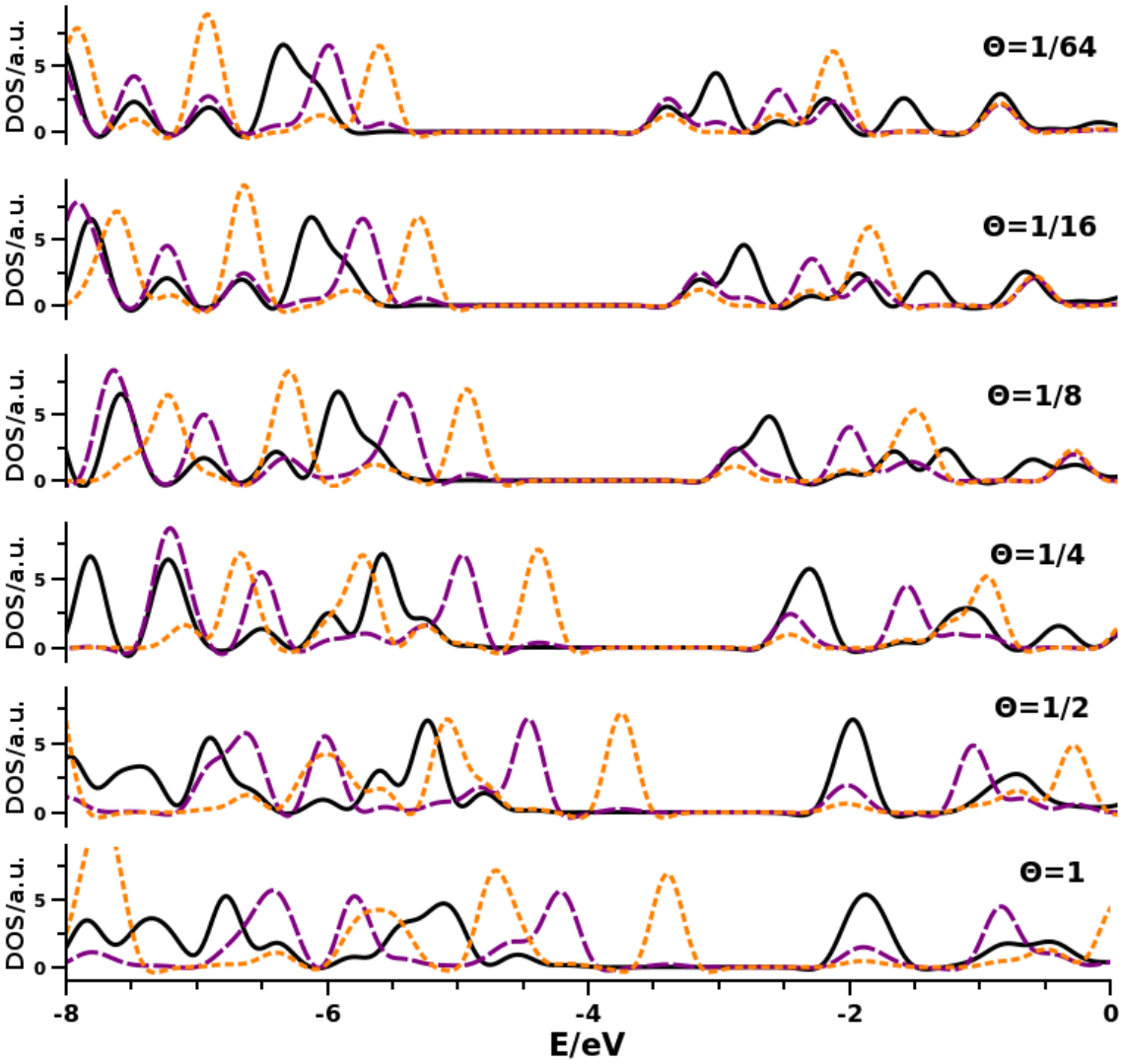

Figure 4.15: Density of states projected on the docking-side ring (black solid line), the middle ring (purple dashed line) and the head-side ring (orange dotted line) of the free-standing 'N-up' terpyrimidinethiol monolayer aligned at the docking-side vacuum level for different coverages

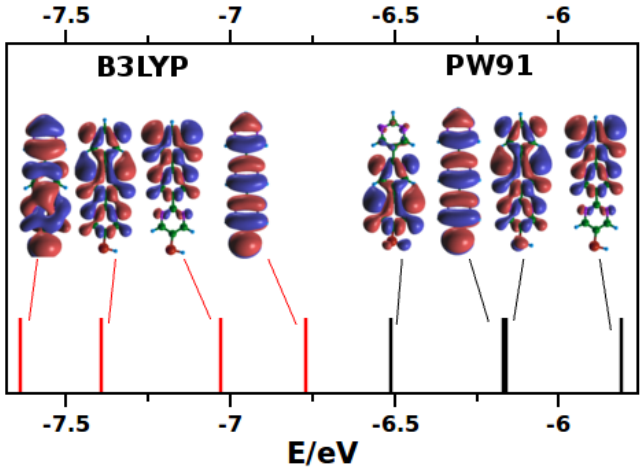

Figure 4.16: Energetic positions and shape of the electronic states of 'N-up' terpyrimidinethiol relative to the vacuum level obtained with PW91PW91 (black lines) and B3LYP (red lines)

mented correlation-consistent polarized basis-sets and increased the polarization starting from double-ζ. Those basis-sets were choosen because the accuracy of the calculation can be increased in a consistent way by just increasing the order of polarization (triple, quadruple-ζ). In this way we can analyse the effect of the basis set on the electronic structure. To investigate the role of the exchange-correlation functional, we choose the PW91PW91 and the B3LYP functional as implemented in **GAUSSIAN03**. The PW91PW91 functional serves as a reference for the **VASP** calculation where also a PW91 XC-functional was applied. The B3LYP functional was choosen to test the effect of exact-exchange on the electronic structure.

Regarding the evolution of the atomic orbitals when expanding the basis set, we found that going from double to triple-ζ results in a minor change ($< 0.05\,\mathrm{eV}$) of the investigated orbital energies for both functionals. Further polarization had no effect on the energetic position of the orbitals. Therefore, we choose to discuss the results obtained with the triple-ζ basis-set.

The black lines in Fig. 4.16 mark the energetic positions relative to the vacuum level of the eigenstates obtained with the PW91PW91 functional. The orbitals associated to that eigenstates are also illustrated. We find those orbitals to be in good agreement with the $\Theta = \frac{1}{64}$ calculation in Fig. 4.12. The orbital ordering and the trend of the relative energetic differences between the orbitals are conserved. The HOMO-1 seems to be more delocalized than in Fig. 4.12, but still with its major part of the density located at the middle ring. From this finding we can conclude that the $\Theta = \frac{1}{64}$ calculation realizes the isolated molecule situation and that no spurious electric fields

are responsible for the high lying σ-states. In fact, also previous studies [49, 50] on the isolated pyrimidine molecule found a σ-state as HOMO. Here, it would be interesting to investigate how the HOMO changes when going from terpyrimidinethiol to monopyrimidinethiol.

The red lines in Fig. 4.16 mark the energetic positions relative to the vacuum level of the orbitals obtained with the B3LYP functional. We find that by using the B3LYP functional, the ordering of the orbitals change: The HOMO is a π-state and appears higher in energy with respect to the σ-states compared to the results obtained with PW91PW91. Moreover, the HOMO-3 which was a localized σ-state within PW91PW91 is found to be another π-orbital within B3LYP. Surprisingly, the difference between the two σ-states is 0.35 eV and 0.36 eV for B3LYP and PW91PW91, respectively. We conclude that the position of the π-state relative to the two σ-states is changed when exchanging the functional.

The result of a functional dependent ordering of the molecular orbitals was reminiscent to the self-interaction error for localized orbitals within GGA. Previous studies [51, 52] could explain wrong orbital ordering by an artifical Coulomb repulsion of the electron from itself [51]. Clearly, that repulsion is strong for highly localized states which are, as a consequence, shifted up in energy [51]. The exact-exchange portion in B3LYP increases the binding energy for localized states and therefore counteracts the self-interaction error [51]. High-lying σ-states can be explained by the self-interaction error within GGA. When exchanging the functional, the energy gap between the two σ-states remains constant. Those orbitals have different localization character and should, therefore, be affected by a different amount of self-interaction error. But the difference in the localization of both orbitals is not pronounced enough to make a general conclusion from that finding.

4.3.4 Conclusion

To summarize, we investigated monolayers formed of terpyrimidine molecules to understand the influence of electric fields in the backbone on the electronic structure of the SAM. The Kohn-Sham gap was found to decrease by an amount of more than 0.7 eV when going from the isolated molecule to the densely packed SAM. We provide a sound explanation in terms of orbitals localized at different sides of the monolayer. The coverage induced shift of those orbitals inherently depends on their spatial position in the SAM. We compared the loosely packed monolayer representing the isolated molecules with calculations on the molecule in gas phase. It was found that the ordering of the orbitals depends on the applied functional. Those finding may be related to the self-interaction error within GGA.

Our investigation was initialized by the observation of an almost constant IP at either the docking- or head-side as a function of the backbone length of

the free-standing monolayer. The position of the nitrogen atoms determined at which side the IP was constant. That puzzle was resolved when assuming localization of the states in the monolayer. This might also be interesting and will be included in an extended version of the text. Furthermore, we plan to investigate the free-standing 'N-down' monolayer and both configurations adsorbed on Au(111).

Chapter 5

Computational solid-state physics II: Transmission, surface DOS and surface band structure

In this chapter we want to go further in the description of a molecular layer on a surface. The theoretical concept of the Green's function is summed up to arrive at a formalism describing electronic transport and transmission at the DFT level based on Ref. [53]. Furthermore, we point out the similarity between the concepts surface DOS, surface band structure and transmission. Those concepts can handle the influence of a semi-infinite substrate on the electronic properties of the adsorbate. The computational implementation of those concepts, which was obtained during a scientific visit to the Humboldt-Universität zu Berlin, is then discussed in detail. We benchmark the computational implementation by calculating the IV-curves for a biphenylthiolate monolayer and compare the results with the literature. Afterwards the transmission and current for a monolayer based on the distributed dipoles approach are calculated, before we end this chapter with preliminary results concerning the surface DOS and surface band structure.

5.1 Green's function techniques

The theoretical fundamentals of calculating the current for nano objects are now discussed. The pathway of the following stems partly from [54]. A very clear discussion of this topic was found in several reviews, books and lectures by Supryo Datta [55, 56, 57, 58]. Also helpful and recommendable are the review papers [59, 60, 61]

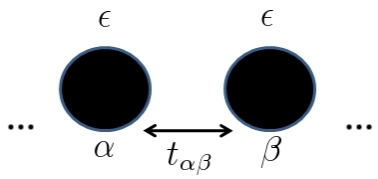

Figure 5.1: On-site matrix elements ϵ and off-site matrix elements $t_{\alpha\beta}$ when describing a linear chain of atoms in the tight-binding approach

Tight-binding Hamiltonian: The tight-binding model is briefly introduced because it is somehow similar to the formalism we want to derive. As the tight-binding model is a semi-empirical model it is, of course, very different from our DFT-based approach. Nevertheless, it might be useful to be introduced to the topic via that model.

The tight-binding or matrix Hamiltonian is determined by inner products of *localized* states ψ_α

$$\mathbf{H}_{\alpha\alpha} = \langle\psi_\alpha|\,\hat{H}\,|\psi_\alpha\rangle = \epsilon_\alpha, \tag{5.1}$$

for the diagonal elements and by

$$\mathbf{H}_{\alpha\beta} = \langle\psi_\alpha|\,\hat{H}\,|\psi_\beta\rangle = t_{\alpha\beta}, \tag{5.2}$$

for the off-diagonal elements. Here one finds the first similarity between the semi-empirical tight-binding approach and the model we choose: We will calculate the Hamiltonian using **SIESTA**. This DFT-code also uses localized states ψ_α (see 2.3).
A nearest neighbor tight-binding model assumes $t_{\alpha\beta} \neq 0$ only for nearest neighboring sites. We, therefore, face a discrete lattice with localized wavefunctions ψ_α at each grid point and the associated Hamiltonian matrix $\mathbf{H}$ Eq. 5.1 and Eq. 5.2:

$$\mathbf{H} = \begin{pmatrix} \epsilon_1 & t_{12} & 0 & 0 & \dots \\ t_{21} & \epsilon_2 & t_{23} & 0 & \dots \\ 0 & t_{32} & \epsilon_3 & \ddots & \ddots \\ 0 & 0 & \ddots & \ddots & \ddots \\ \vdots & \vdots & \ddots & \ddots & \ddots \end{pmatrix}. \tag{5.3}$$

This matrix has the typical tridiagonal form, where only the main diagonal elements and the first diagonal elements below and above the main diagonal are non-zero. If one would also take next-nearest neighbor interactions into account, two more non-zero diagonals would be present. The ϵ_α represent the respective eigenvalue at site α whereas the $t_{\alpha\beta}$ are the coupling or interaction between two sites α and β. For a linear chain of atoms this is schematically illustrated in Fig. 5.1.

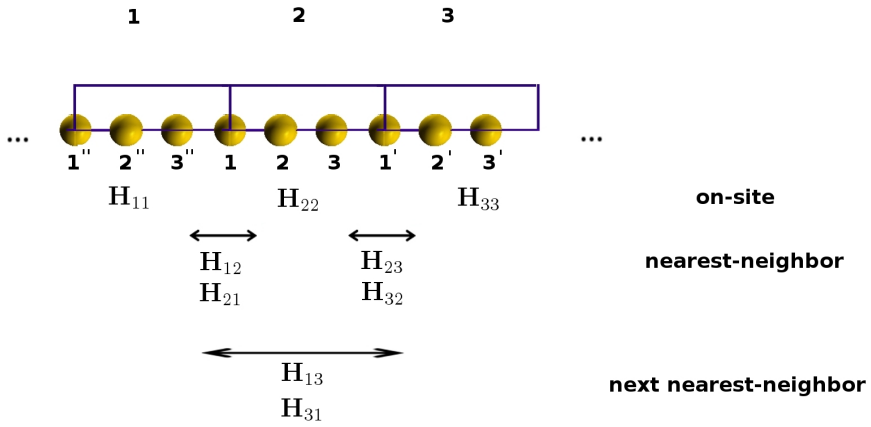

Figure 5.2: The linear chain example in a SIESTA DFT calculation: Overview of the interactions between the indicated unit cells of Au(111), matrices representing them and naming convention

The Hamiltonian in a SIESTA DFT calculation: In the linear chain example Fig. 5.1 each atom was represented by one site. A Hamiltonian with the eigenvalues in the main diagonal and, within the nearest-neighbor approach, the interaction terms between those sites in the first diagonal above and below the main diagonal was obtained. Thinking of a DFT calculation of such a linear chain, the unit cells can also be seen as the sites of interaction. In Fig. 5.2 such an example is illustrated, where the unit-cell contains three Au atoms and is periodically repeated afterwards in a Gedankenexperiment in only one dimension to yield the linear chain. Then, for the Hamiltonian $\mathbf{H}_\mathrm{D}$, one gets a big matrix whose elements are again matrices.
I will try to make this important point clear by considering the case of one-dimensional electrode in Fig. 5.2. A 1D nearest-neighbor tight-binding Hamiltonian in general is written as

$$\mathbf{H}^{(1)}_{\mathrm{total}} = \begin{pmatrix} \mathbf{H}_{11} & \mathbf{H}_{12} & 0 & 0 & \dots \\ \mathbf{H}_{21} & \mathbf{H}_{22} & \mathbf{H}_{23} & 0 & \dots \\ 0 & \mathbf{H}_{32} & \mathbf{H}_{33} & \ddots & \ddots \\ 0 & 0 & \ddots & \ddots & \ddots \\ \vdots & \vdots & \ddots & \ddots & \ddots \end{pmatrix}, \tag{5.4}$$

where the superscript $^{(1)}$ tells us that we consider interaction only with the first neighboring cell.
The α, α elements are the Hamiltonians representing the interaction within each unit cell and the α, β elements the ones representing interaction between unit cells. Comparing Eq. 5.4 with the simple 1D-chain Hamiltonian Eq. 5.3, those are found to be equal with the only difference being the matrix in Eq.

5.4 contains matrices instead of numbers.
We want to further resolve Eq. 5.4 and Fig. 5.2. The element $\mathbf{H}_{22}$ for instance is the matrix representing the interaction in the unit-cell number two. That unit-cell contains the three Au atoms 1, 2 and 3. A general way to write this matrix would be

$$\mathbf{H}_{22} = \begin{pmatrix} \langle\psi_1|\mathbf{H}^{(1)}_{\text{total}}|\psi_1\rangle & \langle\psi_1|\mathbf{H}^{(1)}_{\text{total}}|\psi_2\rangle & \langle\psi_1|\mathbf{H}^{(1)}_{\text{total}}|\psi_3\rangle \\ \langle\psi_2|\mathbf{H}^{(1)}_{\text{total}}|\psi_1\rangle & \langle\psi_2|\mathbf{H}^{(1)}_{\text{total}}|\psi_2\rangle & \langle\psi_2|\mathbf{H}^{(1)}_{\text{total}}|\psi_3\rangle \\ \langle\psi_3|\mathbf{H}^{(1)}_{\text{total}}|\psi_1\rangle & \langle\psi_3|\mathbf{H}^{(1)}_{\text{total}}|\psi_2\rangle & \langle\psi_3|\mathbf{H}^{(1)}_{\text{total}}|\psi_3\rangle \end{pmatrix}. \tag{5.5}$$

We can short the notation in this matrix and write

$$\mathbf{H}_{22} = \begin{pmatrix} h_{1,1} & h_{1,2} & h_{1,3} \\ h_{2,1} & h_{2,2} & h_{2,3} \\ h_{3,1} & h_{3,2} & h_{3,3} \end{pmatrix}. \tag{5.6}$$

The matrices in the other two unit-cells are written in the same way:

$$\mathbf{H}_{11} = \begin{pmatrix} h_{1'',1''} & h_{1'',2''} & h_{1'',3''} \\ h_{2'',1''} & h_{2'',2''} & h_{2'',3''} \\ h_{3'',1''} & h_{3'',2''} & h_{3'',3''} \end{pmatrix} \tag{5.7}$$

and

$$\mathbf{H}_{33} = \begin{pmatrix} h_{1',1'} & h_{1',2'} & h_{1',3'} \\ h_{2',1'} & h_{2',2'} & h_{2',3'} \\ h_{3',1'} & h_{3',2'} & h_{3',3'} \end{pmatrix}. \tag{5.8}$$

Those three matrices are the main diagonal elements in Eq. 5.4. We also need the off-diagonal elements:

$$\mathbf{H}_{12} = \begin{pmatrix} h_{1'',1} & h_{1'',2} & h_{1'',3} \\ h_{2'',1} & h_{2'',2} & h_{2'',3} \\ h_{3'',1} & h_{3'',2} & h_{3'',3} \end{pmatrix}, \tag{5.9}$$

$$\mathbf{H}_{21} = \begin{pmatrix} h_{1,1''} & h_{1,2''} & h_{1,3''} \\ h_{2,1''} & h_{2,2''} & h_{2,3''} \\ h_{3,1''} & h_{3,2''} & h_{3,3''} \end{pmatrix}, \tag{5.10}$$

$$\mathbf{H}_{23} = \begin{pmatrix} h_{1,1'} & h_{1,2'} & h_{1,3'} \\ h_{2,1'} & h_{2,2'} & h_{2,3'} \\ h_{3,1'} & h_{3,2'} & h_{3,3'} \end{pmatrix} \tag{5.11}$$

and

$$\mathbf{H}_{32} = \begin{pmatrix} h_{1',1} & h_{1',2} & h_{1',3} \\ h_{2',1} & h_{2',2} & h_{2',3} \\ h_{3',1} & h_{3',2} & h_{3',3} \end{pmatrix}. \tag{5.12}$$

Those matrices are in the first diagonal above and below the main diagonal in Eq. 5.4. The elements representing the interactions between next-neigboring cells should be zero in a nearest-neighbor approach, $\mathbf{H}_{13} = \mathbf{H}_{31} = 0$.

An important question is how many elements in the off-diagonal matrices $\mathbf{H}_{12}$, $\mathbf{H}_{21}$, $\mathbf{H}_{23}$ and $\mathbf{H}_{32}$ are non zero. For instance, consider the interaction between cell 2 and 3 in Fig. 5.2 and the associated matrix $\mathbf{H}_{23}$: If there is no interaction between atom 1 and $2'$, then $h_{1,2'} = 0$. But then there is also no interaction between atom 1 and $3'$, so $h_{1,3'} = 0$. Then the matrix for interaction between cell 2 and 3 would have the form

$$\mathbf{H}_{23} = \begin{pmatrix} h_{1,1'} & 0 & 0 \\ h_{2,1'} & h_{2,2'} & 0 \\ h_{3,1'} & h_{3,2'} & h_{3,3'} \end{pmatrix}. \tag{5.13}$$

SIESTA constructs a supercell where those standard unit-cells of Fig. 5.2 are incorporated. That supercell is a multiple of the standard unit-cell and is called **Internal auxiliary supercell**. The Internal auxiliary supercell is defined by the sufficient number of replicated unit-cells needed to describe the interactions between atoms of different unit-cells. This is explained by an example, again considering the linear chain built of unit-cells containing three atoms as shown in Fig. 5.2. It is *a priori* not clear, how long the interaction range of one atom is. For the linear chain example in Fig. 5.2 there might, for instance, be an interaction between atom 1 and atom $3'$. Consider the Internal auxiliary supercell to consist of three unit-cells as shown in the picture. If the there is an interaction between atom 1 and atom $3'$ and the Internal auxiliary supercell is only three cells large, then atom 1 has also the possibility of interacting with atom $3'$ ***via* the periodicity** of the Internal auxiliary supercell. This would certainly result in an artificial overlap of interaction and has to be prevented. In that case the Internal auxiliary supercell was choosen to small. SIESTA designes the Internal auxiliary supercell in three dimensions sufficiently large that no such overlap can occur. Then one gets a Hamiltonian describing the interaction in the Internal auxiliary supercell. That Hamiltonian is periodic with respect to the Internal auxiliary supercell.

Matrix Green's function: The consequence of localized states ψ_α (when using a tight-binding model or SIESTA) is that the Hamiltonian $\mathbf{H}$ is described on a grid. We define the retarded one-particle matrix Green's function $\mathbf{G}_\mathrm{R}(E)$:

$$\mathbf{G}_\mathrm{R}(E) = [(E + i\delta)\mathbf{S} - \mathbf{H}]^{-1}. \tag{5.14}$$

The δ means an infinitesimal 0^+, $\mathbf{I}$ is the identity matrix and $\mathbf{S} = \mathbf{S}_{mn} = \langle\psi_m|\psi_n\rangle$ the overlap matrix. The term matrix Green's function refers to the discrete grid the whole problem is formulated on. Eq. 5.14 is very similar

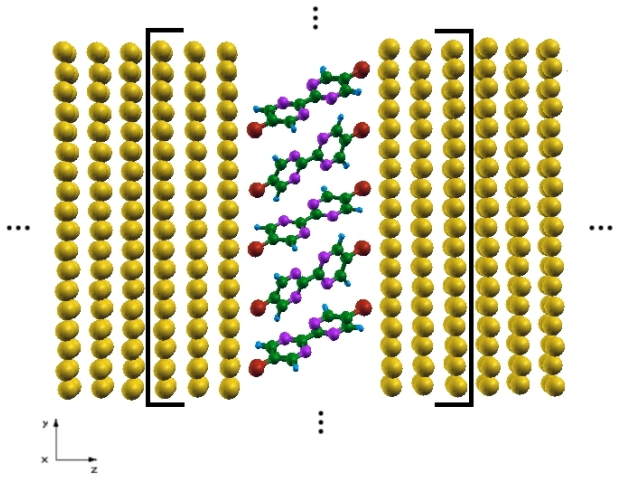

Figure 5.3: The system parted into a device and two electrode regions

to what we have discussed in chapter 3 (see Eq. 3.22) and also stems from the Schrödinger equation. The physical meaning of the Green's function is discussed later. For now its introduction is justified by the fact that one can calculate certain physical properties more easily with the use of Green's function. Fig. 5.3 shows a prototypical molecular device. It can be parted into the left electrode, the central region with the monolayer (also called the device region, or the channel) and the right electrode. The problem is that in z-direction one has a finite object (3 layers of Au, the SAM and again three layers of Au) and two semi-infinite objects (the left and right electrode) coupled to it as indicated in Fig. 5.3. The goal is to incorporate the influence of the infinite electrodes on the finite central region.

To explore how the Green's function works, we consider the central region coupled only to one electrode (see Fig. 5.4). Once the solution to this problem is known, it is applicable to the second electrode and we can solve the 'whole' problem. We can then write the overall Hamiltonian $\mathbf{H}$ of this part of the system as

$$\mathbf{H} = \begin{pmatrix} \mathbf{H}_{\mathrm{D}} & \mathbf{H}_{\mathrm{DL}} \\ \mathbf{H}_{\mathrm{LD}} & \mathbf{H}_{\mathrm{L}} \end{pmatrix}, \tag{5.15}$$

where the subscript D stands for device (*i.e.* the central region) and L for the left electrode. The $\mathbf{H}_{\mathrm{DL,LD}}$ are the coupling matrices of the device to the left electrode and vice versa. This is essentially the same idea we had in the linear chain in the last two paragraphs: First we introduced single atoms as sites of interaction (tight-binding), then unit-cells (SIESTA DFT calculation) and now we want to describe the interactions on- and between device and

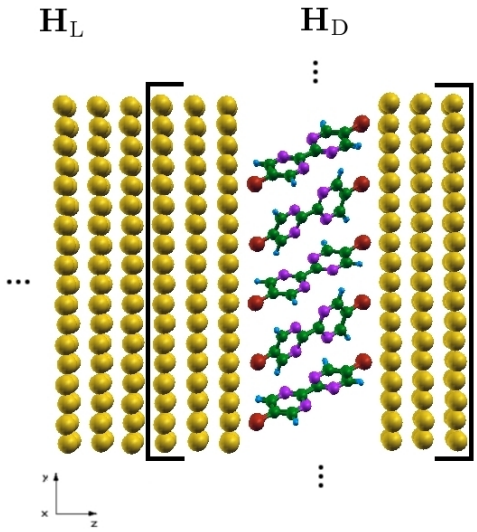

Figure 5.4: One electrode and the device represented by their respective Hamiltonians

electrode that both consist of many atoms and unit-cells.

We can formulate the Green's function $\mathbf{G}$ (we don't denote the subscript R in the following) for this system in the same fashion as the Hamiltonian

$$\mathbf{G} = \begin{pmatrix} \mathbf{G}_\mathrm{D} & \mathbf{G}_\mathrm{DL} \\ \mathbf{G}_\mathrm{LD} & \mathbf{G}_\mathrm{L} \end{pmatrix}, \tag{5.16}$$

where $\mathbf{G}_\mathrm{D}$ is the device's and $\mathbf{G}_\mathrm{L}$ the left electrode's Green's function. From Eq. 5.14 we can write

$$\begin{aligned} \mathbf{G} &= \begin{pmatrix} \mathbf{G}_\mathrm{D} & \mathbf{G}_\mathrm{DL} \\ \mathbf{G}_\mathrm{LD} & \mathbf{G}_\mathrm{L} \end{pmatrix} = \\ &= \begin{pmatrix} (E+i\delta)\mathbf{S}_\mathrm{D} - \mathbf{H}_\mathrm{D} & (E+i\delta)\mathbf{S}_\mathrm{DL} - \mathbf{H}_\mathrm{DL} \\ (E+i\delta)\mathbf{S}_\mathrm{LD} - \mathbf{H}_\mathrm{LD} & (E+i\delta)\mathbf{S}_\mathrm{L} - \mathbf{H}_\mathrm{L} \end{pmatrix}^{-1}. \end{aligned} \tag{5.17}$$

We now make use of the following identity:

If

$$\begin{pmatrix} \mathbf{a} & \mathbf{b} \\ \mathbf{c} & \mathbf{d} \end{pmatrix} = \begin{pmatrix} \mathbf{A} & \mathbf{B} \\ \mathbf{C} & \mathbf{D} \end{pmatrix}^{-1},$$

then

$$\mathbf{a} = \left(\mathbf{A} - \mathbf{B}\mathbf{D}^{-1}\mathbf{C}\right)^{-1}. \tag{5.18}$$

Proof.

$$\rightarrow \begin{pmatrix} \mathbf{a} & \mathbf{b} \\ \mathbf{c} & \mathbf{d} \end{pmatrix} \begin{pmatrix} \mathbf{A} & \mathbf{B} \\ \mathbf{C} & \mathbf{D} \end{pmatrix} = \begin{pmatrix} \mathbf{I} & 0 \\ 0 & \mathbf{I} \end{pmatrix}$$

$$\rightarrow \mathbf{A}\mathbf{a} + \mathbf{B}\mathbf{c} = \mathbf{I}$$

$$\rightarrow \mathbf{C}\mathbf{a} + \mathbf{D}\mathbf{c} = 0$$

$$\rightarrow \mathbf{c} = -\mathbf{D}^{-1}\mathbf{C}\mathbf{a}$$

$$\rightarrow \mathbf{A}\mathbf{a} + \mathbf{B}\left(-\mathbf{D}^{-1}\mathbf{C}\mathbf{a}\right) = \mathbf{I}$$

$$\rightarrow \mathbf{a}\left(\mathbf{A} - \mathbf{B}\mathbf{D}^{-1}\mathbf{C}\right) = \mathbf{I}$$

$$\rightarrow \mathbf{a} = \left(\mathbf{A} - \mathbf{B}\mathbf{D}^{-1}\mathbf{C}\right)^{-1}$$

□

Using the identity Eq. 5.18 we can rewrite the Matrix in Eq. 5.17 and get

$$\begin{aligned} \mathbf{G}_{\mathrm{D}} = \{&(E + i\delta)\mathbf{S}_{\mathrm{D}} - \mathbf{H}_{\mathrm{D}} - \\ &- [(E + i\delta)\mathbf{S}_{\mathrm{DL}} - \mathbf{H}_{\mathrm{DL}}])\mathbf{G}_{\mathrm{L}}^{-1}\left[(E + i\delta)\mathbf{S}_{\mathrm{LD}} - \mathbf{H}_{\mathrm{LD}}\right]\}^{-1}, \end{aligned} \tag{5.19}$$

where

$$\mathbf{G}_{\mathrm{L}} = \left[(E + i\delta)\mathbf{S}_{\mathrm{L}} - \mathbf{H}_{\mathrm{L}}\right]^{-1}. \tag{5.20}$$

We can also define the self-energy matrix here:

$$\mathbf{\Sigma} = [(E + i\delta)\mathbf{S}_{\mathrm{DL}} - \mathbf{H}_{\mathrm{DL}}])\mathbf{G}_{\mathrm{L}}^{-1}\left[(E + i\delta)\mathbf{S}_{\mathrm{LD}} - \mathbf{H}_{\mathrm{LD}}\right] \tag{5.21}$$

and rewrite Eq. 5.19 to obtain

$$\mathbf{G}_{\mathrm{D}} = \left[(E + i\delta)\mathbf{S} - \mathbf{H}_{\mathrm{D}} - \mathbf{\Sigma}\right]^{-1}. \tag{5.22}$$

As we see the self energy describes the influence of the left contact on the device region. Eq. 5.22 means we describe the device by its Hamiltonian and the influence of the electrode by the self-energy.
We will later see that the Green's function of the device Eq. 5.19 is the desired object, once we have $\mathbf{G}_\mathrm{D}$ we can calculate all interesting observables. We are not interested in the reservoir, we only want to know how it acts on the device. From Eq. 5.19 we see that (assuming the Hamiltonian is known) the problem is now reduced to finding the Green's function of the left electrode $\mathbf{G}_\mathrm{L}$. When explaining the computational implementation, we will refer a method to calculate the Green's function of a bulk-electrode.

Physical meaning of the Green's function and the self-energy: The following is partly based on chapter 8 in [55]. Let me start by recapturing the definition of the **retarded** one-particle Green's function:

$$\mathbf{G}^\mathrm{R}(E) = \left[(E + i\delta)\mathbf{S} - \mathbf{H}\right]^{-1}. \tag{5.23}$$

The δ is meant to be an infinitesimal 0^+, $\mathbf{S}$ is the overlap matrix. We will rewrite that equation in matrix form and, for the sake of simplicity, assume we are in an orthogonal basis (the overlap matrix becomes the identity and we only face diagonal elements):

$$\mathbf{G}^\mathrm{R}(E) = \begin{pmatrix} \frac{1}{E-\epsilon_1+i0^+} & 0 & 0 & 0 & \dots \\ 0 & \frac{1}{E-\epsilon_2+i0^+} & 0 & 0 & \dots \\ 0 & 0 & \frac{1}{E-\epsilon_3+i0^+} & \ddots & \ddots \\ 0 & 0 & \ddots & \ddots & \ddots \\ \vdots & \vdots & \ddots & \ddots & \ddots \end{pmatrix}. \tag{5.24}$$

We can introduce the Fourier transform of $\mathbf{G}^\mathrm{R}(E)$ by defining

$$\tilde{\mathbf{G}}^\mathrm{R}(t) = \int \frac{\mathrm{d}E}{2\pi\hbar}\, e^{iEt/\hbar}\, \mathbf{G}_\mathrm{R}(E) \tag{5.25}$$

and find

$$\tilde{\mathbf{G}}^\mathrm{R}(t) = -\frac{i}{\hbar}\Theta(t)e^{-0^+t} \begin{pmatrix} e^{-i\epsilon_1 t/\hbar} & 0 & 0 & 0 & \dots \\ 0 & e^{-i\epsilon_2 t/\hbar} & 0 & 0 & \dots \\ 0 & 0 & e^{-i\epsilon_3 t/\hbar} & \ddots & \ddots \\ 0 & 0 & \ddots & \ddots & \ddots \\ \vdots & \vdots & \ddots & \ddots & \ddots \end{pmatrix}, \tag{5.26}$$

where Θ is the unit-step function. We proof this by considering one level ϵ and performing the inverse Fourier transform:

Proof.

$$\begin{aligned}\mathbf{G}^{\mathrm{R}}(E) &= \int \mathrm{d}t\ e^{iEt/\hbar}\ \tilde{\mathbf{G}}_{\mathrm{R}}(t) \\ &= -\frac{i}{\hbar}\int \mathrm{d}t\ e^{iEt/\hbar}\ \Theta(t)e^{-i\epsilon t/\hbar}e^{-0^+t} \\ &= -\frac{i}{\hbar}\int_0^\infty \mathrm{d}t\ e^{i(E-\epsilon)t/\hbar}e^{-0^+t} \\ &= \frac{1}{E-\epsilon+i0^+}\end{aligned}$$

□

The term retarded refers to the fact that $\tilde{\mathbf{G}}^{\mathrm{R}}(t)$ is zero for $t < 0$. We see that this function satisfies the differential equation

$$\left(i\hbar\frac{\partial}{\partial t} - \epsilon_\alpha\right)\tilde{\mathbf{G}}^{\mathrm{R}}_{\alpha\alpha}(t) = \delta(t), \tag{5.27}$$

or in general (again assuming an orthogonal basis)

$$\left(i\hbar\frac{\partial}{\partial t} - \mathbf{H}\right)\tilde{\mathbf{G}}^{\mathrm{R}}(t) = \mathbf{I}\delta(t), \tag{5.28}$$

which is the time-dependent Schrödinger equation. Thus the retarded Green's function is the response of the system to a perturbation- the matrix element $\tilde{\mathbf{G}}^{\mathrm{R}}_{nm}$ gives the nth component of the wavefunction perturbed at its mth component.
The retardation of this response is plausible. There is, however, a second possible solution

$$\tilde{\mathbf{G}}^{\mathrm{A}}(t) = \left[\tilde{\mathbf{G}}^{\mathrm{R}}(-t)\right]^*, \tag{5.29}$$

called the **advanced** Green's function. It also satisfies the Schrödinger equation, but is zero for all $t \geq 0$. We summarize:

Retarded	Advanced
$\mathbf{G}(E) = [(E+i0^+)\mathbf{I} - \mathbf{H}]^{-1}$	$\mathbf{G}^+(E) = [(E-i0^+)\mathbf{I} - \mathbf{H}]^{-1}$
$\tilde{\mathbf{G}}^{\mathrm{R}}(t) = -\frac{i}{\hbar}\Theta(t)e^{-0^+t}e^{-i\epsilon t/\hbar}$	$\tilde{\mathbf{G}}^{\mathrm{A}}(t) = -\frac{i}{\hbar}\Theta(t)e^{+0^+t}e^{-i\epsilon t/\hbar}$.

(5.30)

The superscript $^+$ in $\mathbf{G}^+(E)$ is in contradiction to the notation in chapter 3, but this is just convention. From the eigenstate representation one may think that the difference between $\mathbf{G}(E)$ and $\mathbf{G}^+(E)$ is minor, since only the infinitesimal (that should be 'physically irrelevant') has a different sign. That

interpretation is cast into doubt by the time-domain representation of the Green's functions: $\tilde{\mathbf{G}}^{\mathrm{R}}(t)$ is a *causal* function and was shown to propagate the inhomogenity caused at time $\delta(t)$, whereas $\tilde{\mathbf{G}}^{\mathrm{A}}(t)$ is a solution to the same differential equation but with no physical initial condition.

To point out the meaning of the self-energy Σ we consider just one level, which means the Hamiltonian reduces to ϵ and we face numbers instead of matrices. The (time-domain) Green's function of the device then has to satisfy the following equation

$$\left(i\hbar\frac{\partial}{\partial t} - \epsilon - \Sigma\right)\tilde{G}^{\mathrm{R}}_{\mathrm{D}}(t) = \delta(t), \tag{5.31}$$

whose solution is

$$\tilde{G}^{\mathrm{R}}_{\mathrm{D}}(t) = \Theta(t)e^{-0^+t}e^{-i\epsilon t/\hbar}e^{-i\Sigma t/\hbar}. \tag{5.32}$$

We will now explore the meaning of the self-energy by rewriting this equation:

$$\begin{aligned}
\tilde{G}^{\mathrm{R}}_{\mathrm{D}}(t) &= \Theta(t)e^{-0^+t}\ e^{-i\epsilon t/\hbar}\ e^{-i\Sigma t/\hbar} \\
&= \Theta(t)e^{-0^+t}\ e^{-i(\epsilon+\Sigma)t/\hbar} \\
&= \Theta(t)e^{-0^+t}\ e^{-i[\epsilon+(\mathrm{Re}\Sigma+i\Im\Sigma)]t/\hbar} \\
&= \Theta(t)e^{-0^+t}\ e^{(-i\epsilon+\mathrm{Re}\Sigma+\Im\Sigma)t/\hbar} \\
&= \Theta(t)e^{-0^+t}\ e^{(-i\epsilon+\mathrm{Re}\Sigma)t/\hbar}\ e^{\Im\Sigma t/\hbar} \\
&= \Theta(t)e^{-0^+t}\ e^{-i\epsilon' t/\hbar}\ e^{-\gamma t/2\hbar},
\end{aligned} \tag{5.33}$$

where $\epsilon' = \epsilon + \mathrm{Re}\Sigma$ and $\gamma = -2\cdot\Im\Sigma$. From this we see the physical meaning of the self-energy Σ: The real part shifts the state from ϵ to ϵ' while the imaginary part gives the state a finite **lifetime**. The latter can be seen by calculating the amplitude of that function, which tells us the probability decay after an initial excitation. We get

$$|\tilde{G}^{\mathrm{R}}_{\mathrm{D}}(t)|^2 \propto e^{-\gamma t/\hbar}, \tag{5.34}$$

where we can indicate the lifetime τ:

$$\frac{1}{\tau} = -\frac{\gamma}{\hbar} = \frac{2\cdot\Im\Sigma}{\hbar}. \tag{5.35}$$

From that equation we can formulate an **uncertainty principle**

$$-\gamma\cdot\tau = 2\cdot\Im\Sigma\cdot\tau = \hbar. \tag{5.36}$$

From quantum mechanics we know the uncertainty for transitions to be $\Delta E = \hbar/\tau$. In our case $2\cdot\Im\Sigma$ appears to play the role of ΔE. That

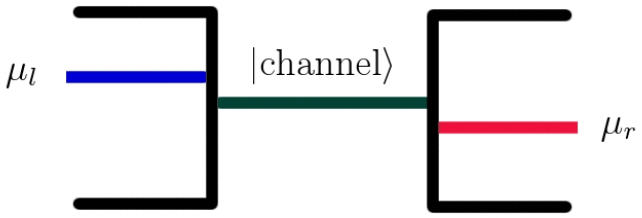

Figure 5.5: Schematic picture of two contacts linked by a single state representing the channel

means, we can 'measure' the states only within a predetermined resolution depending on Σ, *i.e.* the influence of the bulk. A **broadening** in the density of states is the consequence of the self-energy Σ - the more the bulk acts on a state, the less sharp its peak will occur in the density of states. We conclude our discussion of the Green's function by noting that since the Green's function and hence the self-energy are causal functions, the real- and imaginary part of the self-energy are linked by the Hilbert transform $\mathcal{H}$.

5.2 Transmission, surface DOS and surface band structure

In this section further theoretical concepts are illustrated. At first a theoretical framework to calculate IV-curves from the Green's function is introduced. Afterwards we focus on the electronic structure of a surface layer. The concept of the spectral function and two applications, namely the surface DOS and band structure, are discussed.

5.2.1 Transmission and current

We will now calculate the current on an atomic scale. Two main assumptions are made: First coherent transport is considered, meaning that no phase-breaking scattering processes are involved in the description. Second we calculate the zero-bias transmission, meaning we do not account for the effect of the applied voltage on the transmission, i.e. $T(E,V) \approx T(E,0)$. We have to keep in mind that the higher the applied voltage the less a result makes sense [53]. For the derivation of the following formulas we refer to the literature (e.g. [54]) The **Landauer formula** reads [54]

$$I = \frac{2e}{h} \int \mathrm{d}E \, [f(E-\mu_l) - f(E-\mu_r)] \, T(E), \tag{5.37}$$

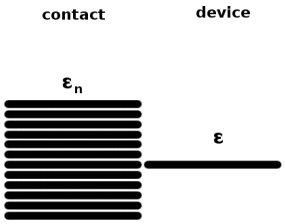

Figure 5.6: A device represented by one single state and a contact by a reservoir of states

where $f(E-\mu_i)$ are Fermi functions describing the contacts. Fig. 5.5 illustrates a single channel and two contacts. From this very schematic picture one can already guess basic priciples of coherent electronic transport.First, from Eq. 5.37, we see that different Fermi levels in the contacts as indicated in Fig. 5.5 are a condition for transport. This is achieved by a bias V_d applied to the contacts, which shifts the Fermi energies by an amount qV_D. If the channel at energy E_{channel} is far below both Fermi energies of the contacts, $f_1(E_{\text{channel}}) = f_2(E_{\text{channel}}) = 1$ and no current will flow. If a channel is far above both Fermi energies, $f_1(E_{\text{channel}}) = f_2(E_{\text{channel}}) = 0$ and no current flows. For a current to flow, the state has to lie in the bias window.

The function $T(E)$ in Eq. 5.37 is called the **transmission function**. It tells us how many states are available at a certain energy and how well the two electrodes are connected. From the Green's function formalism one gets [54]

$$T(E) = \text{Tr}\left[\mathbf{G}_{\text{D}}\mathbf{\Gamma}_l\mathbf{G}_{\text{D}}^{+}\mathbf{\Gamma}_r\right], \tag{5.38}$$

where $\mathbf{\Gamma_i}$ is the **broadening matrix**

$$\mathbf{\Gamma}_{l,r} = i\left[\mathbf{\Sigma}_{l,r} - \mathbf{\Sigma}_{l,r}^{+}\right]. \tag{5.39}$$

The effect of $\mathbf{\Sigma}_i$ is to broaden and shift the states of the device as was shown before.

5.2.2 Surface density of states

In DFT calculations the density of states of a monolayer on a surface is broadened artificialy. A real broadening of the DOS is well described in the Green's function formalism. Through the last sections a single state and one contact like in Fig. 5.6 were frequently used to explain the physical situation. The essence is the same, for a nano device with many states we just get matrices instead of numbers. The coupling of a second contact to the device results in the same processes as coupling only one to it.

Therefore I will try to make the concept of a broadened DOS more clear by discussing the single state example in Fig. 5.6. This subsection follows

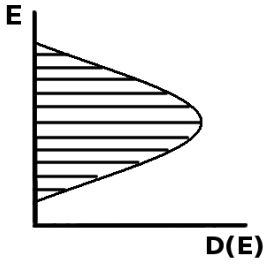

Figure 5.7: Broadened DOS due to the coupling of device and contact

chapter 8.2 in [55]. The total DOS of this system when device and contact are not coupled is

$$D(E) = \delta(E - \epsilon) + \sum_n \delta(E - \epsilon_n), \tag{5.40}$$

which is what we see in Fig. 5.6, where the ϵ_n are the energies of the states in the reservoir and the ϵ is the energy of the device's state. If we couple device and contact, the device's DOS gets broadened. Here we introduce the **local density of states LDOS**, which in general reads

$$D(\boldsymbol{r}; E) = \sum_\alpha |\phi_\alpha(\boldsymbol{r})|^2 \delta(E - \epsilon_\alpha). \tag{5.41}$$

The ϕ_α are the states associated to the energy levels ϵ_α. The LDOS weights the DOS with the spatial probability density of the states. The LDOS can be applied to the situation of a decoupled device and contact (see Fig. 5.6). Then the LDOS for the device would be

$$D(\boldsymbol{r}; E) = \sum_\alpha |\phi_\alpha(\boldsymbol{r})|^2 \delta(E - \epsilon_\alpha) = \delta(E - \epsilon), \tag{5.42}$$

because the only state present in the device is that associated to the energy level ϵ of the device itself (see Fig. 5.6). When device and contact are coupled, states of the reservoir are allowed to leak into the channel and vice versa. Therefore, also states at different energy levels than the primal ϵ of the isolated channel will have a certain amount of spatial probability density within the channel. This is exactly what the LDOS in Eq. 5.41 takes into account: It weights each δ-peak from the uncoupled DOS by the spatial probability density of the associated states and results in a spatial resolved DOS. After being coupled to the reservoir the channel's DOS is broadened as shown in Fig. 5.7.

The LDOS in Eq. 5.41 represents the diagonal elements (divided by a constant) of a more general function called **spectral function**

$$A(\boldsymbol{r}, \boldsymbol{r}'; E) = 2\pi \sum_\alpha \phi_\alpha(\boldsymbol{r}) \delta(E - \epsilon_\alpha) \phi_\alpha^*(\boldsymbol{r}'). \tag{5.43}$$

The spectral function provides the LDOS in any basis. There is an analogue between the LDOS and the electron density $n(\boldsymbol{r})$. The electron density $n(\boldsymbol{r})$ also represents the diagonal elements of a more general quantity called the density matrix

$$\rho(\boldsymbol{r}, \boldsymbol{r}') = \sum_{\alpha} \phi_{\alpha}(\boldsymbol{r}) f_0(\epsilon_{\alpha} - \mu) \phi_{\alpha}^*(\boldsymbol{r}'). \tag{5.44}$$

Just as the sum over the electron density $n(\boldsymbol{r})$ gives the total number of electrons, the sum over $D(\boldsymbol{r}; E)$ gives the density of states $D(E)$. The sum over diagonal elements is the trace and we can note

$$D(E) = \frac{1}{2\pi} \mathrm{tr}\left(A(\boldsymbol{r}, \boldsymbol{r}'; E)\right). \tag{5.45}$$

By knowing the spectral function one gets the DOS and LDOS. We now illustrate that the spectral function can be obtained by using Green's function (again assuming an orthogonal basis for simplicity): One can show [55] that the density matrix $\rho(\boldsymbol{r}, \boldsymbol{r}')$ can be written as

$$\rho = f_0(\mathbf{H} - \mu \mathbf{I}), \tag{5.46}$$

which by comparing Eq. 5.43 and 5.44 leads us to a similar representation for the spectral function:

$$\mathbf{A} = 2\pi\delta(E\mathbf{I} - \mathbf{H}). \tag{5.47}$$

The δ-function can be rewritten

$$2\pi\delta(x) = \left[\frac{1}{x + i0^+} - \frac{1}{x - i0^+}\right] i = \ldots = \frac{2 \cdot 0^+}{x^2 + (0^+)^2}, \tag{5.48}$$

which we use for Eq. 5.47 to get

$$\mathbf{A} = i\left[\left(E + i0^+\right)\mathbf{I} - \mathbf{H})\right]^{-1} - i\left[\left(E - i0^+\right)\mathbf{I} - \mathbf{H})\right]^{-1}. \tag{5.49}$$

We can identify the Green's function in that equation and rewrite the spectral function again making use of Eq. 5.30 to finally get

$$\mathbf{A} = i\left[\mathbf{G} - \mathbf{G}^+\right]. \tag{5.50}$$

The Green's function is directly related to the spectral function, the DOS and LDOS!

A Green's function representation of the DOS was derived. Starting at the LDOS, we showed that knowing the Green's function means knowing all the eigenvalues. Moreover we can calculate a basis-resolved eigenvalue spectrum in any basis. This is of particular interest. One can, of course, use another basis and not the position states in Eq. 5.41. For example, when using atomic orbitals, one can resolve the DOS regarding the atomic orbitals. We call that the **projected density of states PDOS**. The advantage is that one starts from the Green's function that includes the influence of a semi-infinite bulk.

5.2.3 Surface band structure

In our DFT calculations the k-points are uniformly distributed. Clearly that sampling is designed to result in an accurate description of the system and the observables - density matrix, ground-state energy, DOS and so on. It would be nice, to conserve that high accuray of the standard DFT calculation, but calculate the DOS at *arbitrary* k-points (and not at the k-points associated to that accuracy, *i.e.* the uniformly distributed one). Of particular interest are k-points representing high-symmetry lines in the electronic band structure. Then one gets a DOS at every k-point of a band structure. That band structure is not represented by points in an Ek-relationship, it is really more a 3D band structure with a DOS at each coordinate (k_i, E_i). That band structure yields information beyond the dispersion of the electrons: The height, *i.e.* the DOS at each k-point, corresponds to the broadening - if we would have an isloated and unperturbed state, the DOS would be a δ-peak. Once that state is perturbed by a self-energy, it has the chance to leave which results in a finite lifetime, a broadened and smaller peak in the DOS.

In the next section I will outline the computational implementation of the tranmission, surface DOS and surface band structure.

5.3 Computational implementation

The following will guide through our computational realization of the Green's function technique. Those programs were developed in a collaboration with Georg Heimel from the Humboldt Universität zu Berlin who designed most of the codes.

How to build a molecular device: To build a molecular device we first have to build the central region (see Fig. 5.8) To do so, we performed a surface calculation in VASP using the external tool GADGET. Usually one would therefore consider a slab with three layers of Au(111) and the SAM on top of it. We have, however, performed the calculation using five layers of Au(111) for another purpose and therefore started from this geometry. In both ways one gets a S docking-site. We assumed that the S atoms adsorb in the same way at the left- and right electrode. We know the docking geometry from the surface calculation and therefore can apply it to the second electrode. This is realized by adding three more layers of Au(111) (ABC stacking) on the opposed side of the adsorbed SAM after the geometry optimization is done. The tilt angle of the molecules has to be modified to realize that the S atoms on both sides of the monolayer adsorb in the same way. The unit-cell has to be choosen in a way that the Au(111) inter-layer difference to the consecutive periodic Au(111) layer is realized. As already mentioned it is possible to calculate the PDOS, *i.e.* the DOS projected on atomic orbitals. In this

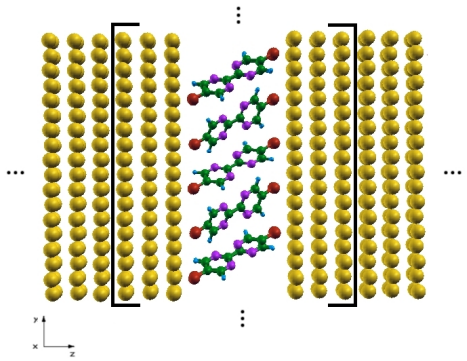

Figure 5.8: The molecular device is parted into two semi-indinite electrodes and the central region with the molecular part and three layers of Au(111) on each side

way we would like to resolve the DOS of each part in the central region. For example, it would be nice to distinguish between the layers of Au(111) and the molecular part sandwiched between the two electrodes. To do so we project the DOS on atomic orbitals associated to the part where we want to know the DOS. It is important to sort the atoms in the unit-cell according to their position in z-direction from low to high. Then one can project the DOS on each layer of the central region.

The 'rest' of the semi-infinite electrodes on each side of the central region is added by a self-energy formalism based on the theoretical basics explained in 5.1. We therefore have to build a unit-cell for the bulk-electrode. This unit-cell contains three layers of Au(111) that have to be sorted in exactly the same way as in the central region.

The pathway to calculate $T(E)$ and the current: To get an overview the pathway to get the transmission is outlined. The input needed are the Green's function of the device 5.22 and therefore the self-energy $\mathbf{\Sigma}$.

From Eq. 5.22, we see that we need to know the device's Hamiltonian matrix $\mathbf{H}_\mathrm{D}$ and the overlap matrix $\mathbf{S}$. Therefore we perform a SIESTA DFT calculation on the central region of the device we built. By using a modified *pdosk.F* file we force SIESTA to write out the Hamiltonian and the overlap matrix at every k-point. To enable this mechanism, one has to adjust the parameter *nhist* in the SIESTA *.fdf* file. In that file one can find a block responsible for the PDOS:

```
$ grep -B 2 'endblock Projected' biphen.fdf
%block ProjectedDensityOfStates
 -10.0  5.0  0.2  1503  eV
```

```
%endblock ProjectedDensityOfStates
```

The last number before eV is the parameter *nhist*. By setting ***nhist*=1503** one specifies a central region calculation and the Hamiltonian and overlap matrices are written to files

Then one needs to calculate the overlap and Hamiltonian matrix for the electrode. Therefore a SIESTA DFT calculation on the unit-cell with three layers of Au(111) which we built in the last paragraph is performed. By setting ***nhist*=1502** one gets the Hamiltonian and overlap matrices for the electrode.

For both this calculations an input file named ***params.inp*** is needed. In this input file one has to write the number Internal auxiliary supercell. The Internal auxiliary supercell was already discussed in paragraph 5.1. It is the supercell of periodicty for the Hamiltonian and calculated by SIESTA. One finds it in the outfile of a SIESTA calculation as quoted below

```
$ grep 'Internal auxiliary supercel' bulk.out
superc: Internal auxiliary supercell:     3 x     3 x     2
```

Those three numbers determine the **'Internal auxiliary supercell'**, have to be written into a file ***params.inp*** before starting the respective SIESTA calculations. An example for a *params.inp* file is quoted below:

```
$more params.inp
SuperCellX 5
SuperCellY 3
SuperCellZ 1
```

Note: The way we've implemented the scheme so far can only handle SuperCellZ = 2 or 3 for the bulk calculation. If SuperCellZ = 4 only next-nearest neighbour interaction between unit-cells is taken into account.

The program *transmission.f90* iteratively calculates the self-energy. The algorithm is based on the idea of the Green's function introduced in the last sections. The program needs the Hamiltonian and overlap matrices of the electrode and central region one gets from the SIESTA DFT calculation. In *transmission.f90* we make use of an algorithm introduced in [62, 63]. When the Σs are calculated, the device's Green's function $\mathbf{G}_\mathrm{D}$ Eq. 5.22 and the $\mathbf{\Gamma}$s Eq. 5.39 are determined. We then compute the transmission using Eq. 5.38 and are done.

transmission.f90 performs that procedure for every k-point. For every k-point it needs an input file named *transmission.inp.spin1.00<kpoint>*. To produce those input files we used the following script (for 24 k-points in our case):

```
#!/bin/bash
2
for (( i=1; $i <= 24; i++ ))
4 do
echo "SpinKpoint              1 $i">transmission.inp.spin1.00$i
6 echo "MinMaxStepEne          -3.0 3.0 0.01
ElectrodeFermi          -2.5503
8 CentralRegionFermi    -3.7851
ClipWings               450
10 EpsilonIteration     1.e-10
DeltaImaginary          1.0e-5
12 StartStopDos_01      1    90
StartStopDos_02         91 180
14 StartStopDos_03      181 270
StartStopDos_04         271 674">>transmission.inp.spin1.00$i
16 done
```

Line 6 determines the range in energy for calculating the transmission and the discrete steps. Line 7 and 8 are the Fermi energies of the central region and the electrode found in the output of each SIESTA calculation. We don't want to consider the central region's interaction with its consecutive images, we add the semi-infinite bulk instead. Therefore, one has to open the file *CheckWings.dat* in the directory of the central region DFT calculation. There one sees the first rows of the Hamiltonian, where (somewhere in the middle of the matrix) the elements become zero and then again nonzero. One has to pick a number in the range where everything is zero to clip the interactions going beyond the unit-cell of the central region. That number has to be written to Line 9. Line 10 and 11 are the convergence criteria for the Σ iteration and the δ needed for the retarded Green's function of the device Eq. 5.22. The last lines determine the atomic orbitals the density of states is projected on.

To calculate the transmission one could use a script

```
#!/bin/bash
2
for (( i=1; $i <= 24; i++ ))
4 do
transmission<transmission.inp.spin1.00$i>
6 transmission.out.spin1.00$i
done
```

where line 3 is a loop over the number of k-points. As an output one gets the transmission for each k-point listed below:

```
$ ll transmission.spin1.0*
-rw-r--r-- 1 david david 66711 2010-03-04 09:10 transmission.spin1.001
-rw-r--r-- 1 david david 66711 2010-03-04 09:57 transmission.spin1.002
-rw-r--r-- 1 david david 66711 2010-03-04 10:44 transmission.spin1.003
-rw-r--r-- 1 david david 66711 2010-03-04 11:32 transmission.spin1.004
-rw-r--r-- 1 david david 66711 2010-03-04 12:19 transmission.spin1.005
-rw-r--r-- 1 david david 66711 2010-03-04 13:06 transmission.spin1.006
-rw-r--r-- 1 david david 66711 2010-03-04 13:53 transmission.spin1.007
-rw-r--r-- 1 david david 66711 2010-03-04 14:40 transmission.spin1.008
-rw-r--r-- 1 david david 66711 2010-03-04 15:28 transmission.spin1.009
-rw-r--r-- 1 david david 66711 2010-03-04 16:15 transmission.spin1.010
-rw-r--r-- 1 david david 66711 2010-03-04 17:03 transmission.spin1.011
-rw-r--r-- 1 david david 66711 2010-03-04 17:50 transmission.spin1.012
-rw-r--r-- 1 david david 66711 2010-03-04 18:37 transmission.spin1.013
-rw-r--r-- 1 david david 66711 2010-03-04 19:25 transmission.spin1.014
-rw-r--r-- 1 david david 66711 2010-03-04 20:12 transmission.spin1.015
-rw-r--r-- 1 david david 66711 2010-03-04 21:00 transmission.spin1.016
-rw-r--r-- 1 david david 66711 2010-03-04 21:47 transmission.spin1.017
-rw-r--r-- 1 david david 66711 2010-03-04 23:18 transmission.spin1.018
-rw-r--r-- 1 david david 66711 2010-03-04 23:18 transmission.spin1.019
-rw-r--r-- 1 david david 66711 2010-03-04 19:11 transmission.spin1.020
-rw-r--r-- 1 david david 66711 2010-03-04 19:58 transmission.spin1.021
-rw-r--r-- 1 david david 66711 2010-03-04 20:46 transmission.spin1.022
-rw-r--r-- 1 david david 66711 2010-03-04 21:33 transmission.spin1.023
-rw-r--r-- 1 david david 66711 2010-03-04 22:20 transmission.spin1.024
```

As you see, the tranmission was calculated using unrestricted spin. Each file carries the transmission and the PDOS for the energy range you specified:

```
$ more transmission.spin1.001
-3.0000000000   0.0313415051        0.1319394856        0.1490514420        0.1845801541        0.0430935056
-2.9900000095   0.0312860399        0.1367842169        0.1584191207        0.1942537757        0.0447129078
-2.9800000191   0.0312665433        0.1429603410        0.1690557671        0.2058608908        0.0468657931
-2.9699997902   0.0313670754        0.1497922572        0.1794440452        0.2173130298        0.0495214185
-2.9600002766   0.0315128863        0.1554951679        0.1869733049        0.2249024996        0.0524357545
-2.9500002861   0.0307040215        0.1572128023        0.1887304298        0.2245544587        0.0531632030
-2.9400000572   0.0281045824        0.1525381452        0.1813469500        0.2130226518        0.0475036274
-2.9300000668   0.0265230596        0.1448648720        0.1693718034        0.1970108506        0.0412249815
-2.9200000763   0.0266638398        0.1576283710        0.1787768419        0.2018523997        0.0427065279
-2.9099998474   0.0260734409        0.1704712437        0.1869323985        0.2055662049        0.0433632383
```

We now have to integrate over the Brillouin-zone, *i.e.* sum the files up

$$T(E) = \sum_k T_k(E), \tag{5.51}$$

where we used GNU octave as it is perfectly suited for such matrix operations. According to Eq. 5.37 we can now calculate the IV-curve.

To conclude this paragraph an overview of the steps that are necessary to obtain the tranmission is given:

1. **SIESTA DFT calculation of the electrode:**
   - *params.inp* with proper Internal auxiliary supercell
   - *nhist*=1502
   - Hamiltonian and overlap matrices are written to one file
2. **SIESTA DFT calculation of the central region:**
   - *params.inp* with proper Internal auxiliary supercell
   - *nhist*=1503
   - Hamiltonian and overlap matrices are written to one file

3. **Calculate $T(E)$**

   - Collect the output files of the central region and electrode calculations
   - Produce the input file for every k-point (set the Fermi energies, clip the wings, set the convergence criteria and the orbitals for the PDOS
   - Start the calculation of $T(E)$ by using the program *transmission.f90*
   - $\sum_k T_k(E)$

4. **Calculate the current on an atomic scale using Eq. 5.37**

Calculating the surface DOS: The tranmission and surface DOS are very similar. This is also obvios from the fact that we discussed a device with two contacts by considering a device with only one contact, which is in fact a surface with a molecular layer on it.

From this point of view, also the computational implementation is quite similar to that of the transmission. We again have to find the self-energy of the Au(111) bulk (therefore we need the Hamilton- and overlap matrices of the bulk), set up the Green's function (therefore we need the Hamilton- and overlap of the surface region) and calculate the DOS (by taking the trace of the anti-hermitian part of the Green's function), which is broadened according to the influence of the bulk. The surface region calculation is performed using a preconverged geometry (in VASP and GADGET) where 5 layers and two organic molecules in the unit cell represent the Au(111) surface with the adsorbed monolayer. We add three layers of Au(111) to the tail of that slab and then have 8 layers of Au and the molecules in the unit cell of the surface-region DFT calculation. We then calculate the self-energy and its influence on the surface region: We 'append' the bulk to the surface region, *i.e.* exchanging the three layers of Au we've added before by an infinite bulk as shown in Fig. 5.9. After that we are able to compute the spectral function and the LDOS as explained before. Again, we can calculate the PDOS and project the DOS on different layers of the surface region. The following steps summarize the surface DOS calculation:

1. **SIESTA DFT calculation of the electrode:**

   - *params.inp* with proper Internal auxiliary supercell
   - *nhist*=1502
   - Hamiltonian and overlap matrices are written to one file

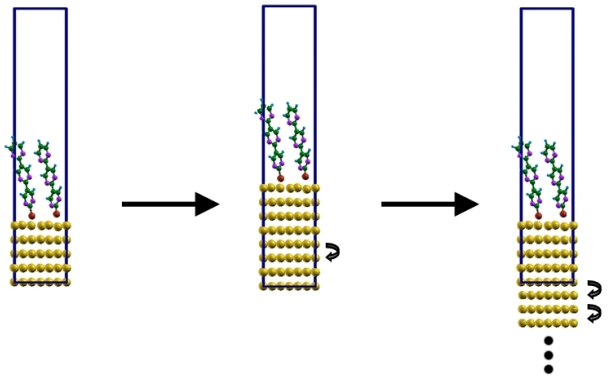

Figure 5.9: Influence of an infinite bulk added to the surface region

2. **SIESTA DFT calculation of the surface region:**
   - add three layers of Au (111) to your preconverged surface calculation
   - *params.inp* with proper Internal auxiliary supercell
   - *nhist*=1504
   - Hamiltonian and overlap matrices are written to one file
3. **Calculate** $D(E)$
   - Collect the output files of the surface region and electrode calculations
   - Produce the input file for every k-point (set the Fermi energies, set the convergence criteria and the orbitals for the PDOS
   - Start the calculation of $D(E)$ by using the program *surfacedos.f90*
   - $\sum_k D_k(E)$

The program *surfacedos.f90* also needs the input files for every k-point. We produced the input files with the following script:

```
#!/bin/bash

for (( i=1; $i <= 24; i++ ))
do
echo "SpinKpoint              1 $i">surfacedos.inp.spin1.00$i
echo "MinMaxStepEne           -5.0 3.0 0.01
BulkFermi               -2.5503
SurfaceFermi            -3.7532
EpsilonIteration        1.e-10
DeltaImaginary          1.0e-5
```

```
11 StartStopDos_01      1  90
   StartStopDos_02      91  180
13 StartStopDos_03      181  270
   StartStopDos_04      271  360
15 StartStopDos_05      361  450
   StartStopDos_06      451  838">>surfacedos.inp.spin1.00$i
17 done
```

The lines were already explained in the last section. The result of calculating the surface LDOS at every k-point are files with the bulk-broadened LDOS projected on the specified

Calculating the surface band structure For the surface band structure SIESTA is forced to write out the Hamiltonian and overlap matrices at arbitrary k-points. We want to conserve the high accuracy of the calculation obtained with a uniformly sampled k-point grid. Therefore we perform a DFT calculation on the surface and the bulk-electrode. Then one performs a calculation where the written density matrix needs to be read in by setting *DM.UseSaveDM* to *.true.* in the *.fdf* file. Then we set *MaxSCFIterations* to *1* meaning that SIESTA reads in the density matrix and does exactly nothing. The *pdosk.F* routine was modified in a way that when *nhist=1505* and a file named ***kpoints.inp*** is present, the Hamiltonian and overlap matrices are written to file for that k-points. The number of k-points has to be in the first row of *k-points.inp* followed by the k-points in $k_x\, k_y\, k_z$ format. The following steps summarize the surface bands calculation:

1. **SIESTA DFT calculation of the electrode:**
   - *params.inp* with proper Internal auxiliary supercell
   - *nhist*=1505
   - *DM.UseSaveDM* .true.
   - *MaxSCFIterations* 1
   - *kpoints.inp* with number of k-points and k-points
   - Hamiltonian and overlap matrices are written to one file
2. **SIESTA DFT calculation of the surface region:**
   - add three layers of Au (111) to your preconverged surface calculation
   - *params.inp* with proper Internal auxiliary supercell
   - *nhist*=1505
   - *DM.UseSaveDM* .true.

- *MaxSCFIterations* 1
- *kpoints.inp* with number of k-points and k-points
- Hamiltonian and overlap matrices are written to one file

3. **Calculate** $D(E)$
   - Collect the output files of the surface region and electrode calculations
   - Produce the input file for every k-point (set the Fermi energies, set the convergence criteria and the orbitals for the PDOS
   - Start the calculation of $D(E)$ by using the program *surfacedos.f90*

One ends up with a file for every specified k-point. Those files contain the DOS as a function of the energy for the specified atomic orbitals. Therefore we can plot a three dimensional band structure.

5.4 Results and Discussion

Distributing polar groups along the backbone has been shown to critically influence the metal/organic interface (see 4.2. The electronic structure of the compound metal/monolayer system was found to be significantly different when the monolayer was built of polar units. In this section we continue our investigation of polar backbones in a SAM by exploring how they behave as molecular-electronic devices. We therefore calculate the transmission and IV-characteristics of prototypical examples. Furthermore, as an illustration, the concepts of the surface DOS and band structure are applied to those systems. This section is started by testing our approach for a monolayer device based on a biphenyldithiolate SAM.

5.4.1 Transmission benchmark - the biphenyldithiolate SAM

The biphenyldithiolate SAM in Fig. 5.10 was choosen as the reference system to test our computaional implementation because i) it served as a reference system in previous publications of our group (*e.g.* [21]) and ii) it was already considered as a molecular device in the literature [64].

Fig. 5.4.1 compares the transmission function obtained by Kim *et. al* in Ref. [64] and our results. The authors in Ref. [64] have calculated the transmission per molecule, whereas we calculate the transmission per unit-cell. As there are two molecules in the unit-cell, the two plots differ by a factor of 2. Besides that the agreement is very good. The influence of different tilt angles of the long molecular axis was considered in Ref. [64]

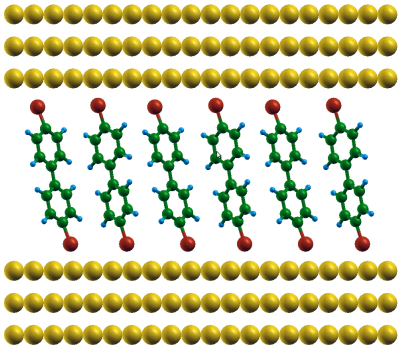

Figure 5.10: The biphenyldithiol SAM - the reference device to test our methodology

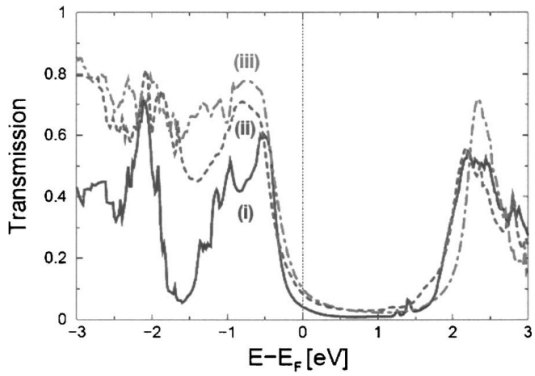

(a)

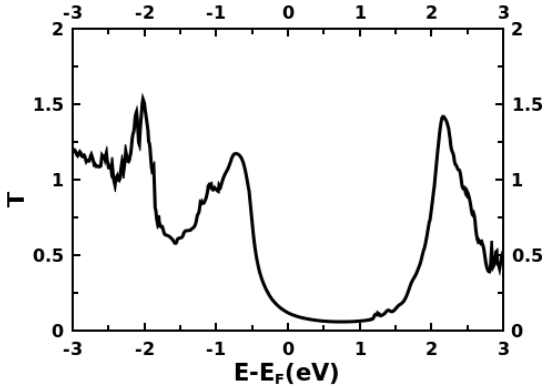

(b)

Figure 5.11: Comparison of the transmission function: (a) Fig. 8 in Ref.[64] where the three curves represent different tilt angles (see text) (b) The transmission function calculated for biphenyldithiolate

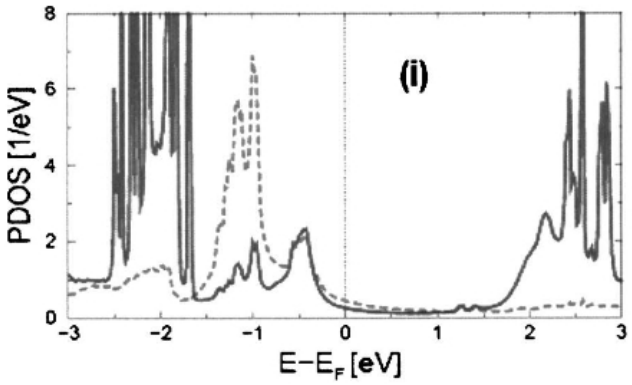

(a)

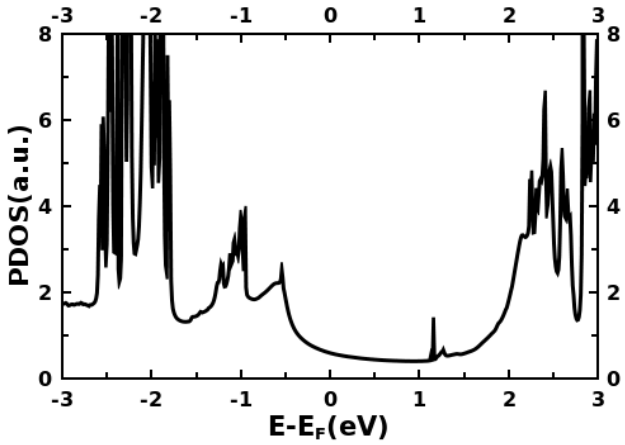

(b)

Figure 5.12: Comparison of the DOS projected onto the molecular part of the junction: (a) Fig. 7 in Ref.[64] (b) The PDOS calculated for biphenyldithiolate

, hence the three curves in Fig. 5.4.1. Curve I corresponds to $\Theta = 15\,^{\circ}$, curve II to $\Theta = 30\,^{\circ}$ and curve III to a parallel arrangement of the molecules relative to each other. The agreement seems to be good with curve I and II, maybe the best with curve I (a tilt of $\gamma = 14.4^{\circ}$ was measured for our biphenyldithiolates).

The comparison of the DOS projected onto the molecular orbitals shown in Fig. 5.4.1 is also very good. Here only the $\Theta = 15\,^{\circ}$ curve of Ref. [64] is plotted. μ Moreover, we compare the IV-characteristics in Fig. 5.4.1. There, we also find a similar result compared to Ref. [64] . Again, curve I represents a tilt angle of $\gamma = 15^{\circ}$.

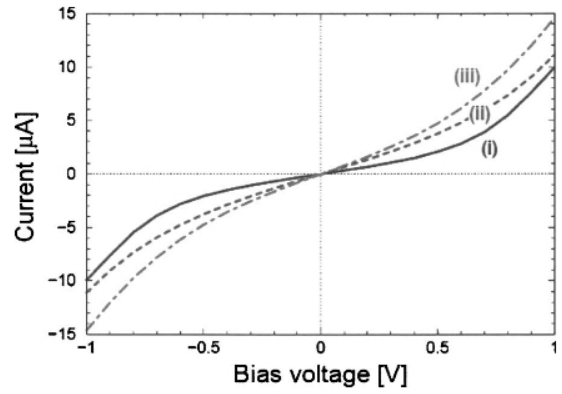

(a)

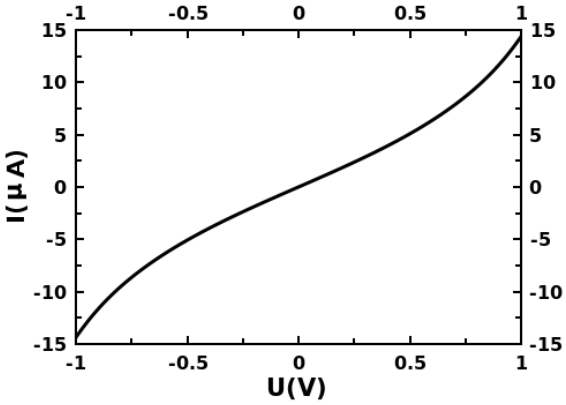

(b)

Figure 5.13: Comparison of the IV-characteristics: (a) Fig. 9 in Ref.[64] (b) The current calculated for biphenyldithiolate

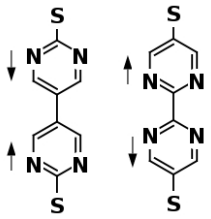

Figure 5.14: The 5,5'-bipyrimidine-2,2'-dithiolate (N-out) and the 2,2'-bipyrimidine-5,5'-dithiolate (N-in) SAM-forming molecule

5.4.2 Distributing dipoles in a molecular device

As a next step we combine our approach of distributing the dipoles with the transport formalism derived so far. The actual position of polar groups within the backbone affected the electrostatic properties of the monolayer. Two pyrimidinethiol molecules that differ in the position of the nitrogens only (and therefore were named 'N-up' and 'N-down') behave completely different when assembled into a SAM. In detail, the level alignment was by an amount of more than 0.7 eV different in those structures, as discussed in detail in section 4.2.

Building on that finding we investigated two different bipyrimidinedithiolate based SAMs: A 5,5'-bipyrimidine-2,2'-dithiolate and a 2,2'-bipyrimidine-5,5'-dithiolate based SAM (see Fig. 5.14), referred to as 'N-out' and 'N-in', were considered as active elements in the junction.

We would expect those two molecules to behave different as a conductor: Considering the collective electrostatics in the monolayer one might expect that the N-out configuration should have lower lying states compared to N-in. Different transmission and IV-characteristics should be the consequence as also the transport channels are concerned. Indeed, this was found when calculating the IV-characteristics as shown in Fig. 5.15 - the two currents differ significantly! In the high-bias regime above $1\,V$ the current for both configuration might differ even more. To investigate the high-bias regime one would have to perform non-equillibrium Green's function calculations. A tranmission and PDOS obtained within the zero-bias approximation cannot be used for calculating the current in the high-bias regime [53].

Also the transmission and PDOS shown in Fig. fit in that picture of higher and lower lying states - the occupied orbitals of the N-in monolayer are closer to the Fermi level than the orbitals of the N-out monolayer as originally expected. An aspect that requires further attention is that the transmission spectrum in Fig. 5.4.1 is higher than 2. The reason is that 3 eV below the Fermi level more than one state is available for transport in the unit-energy intervall.

The explanation of the different transport characteristics for the N-in and

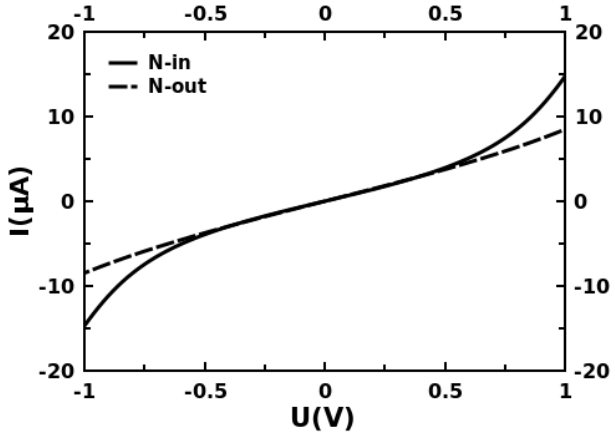

Figure 5.15: The current as a function of the voltage for N-in (solid line) and N-out (dashed line)

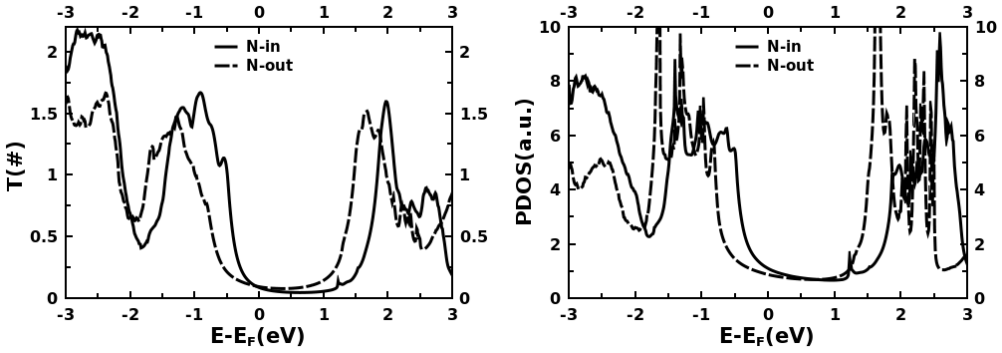

(a) (b)

Figure 5.16: Transmission (a) and PDOS (b) for N-in (solid line) and N-out (dashed line)

N-out confirmation as a result of the collective behaviour of the polar parts in a SAM can now be tested. For this to be the case, the shifts in the PDOS (and transmission) between 'N-in' and 'N-out' have to be significantly larger than the differences in the molecular HOMO energies. Therefore, we performed GAUSSIAN calculations to obtain the HOMO energies[1] of the 'N-in' and 'N-out' molecule. The HOMO energies in the molecular calculations are important as we also consider them in the DFT calculation of the device. The PW91PW91 functional was applied to ensure comparability with the SIESTA DFT calculations, and the standard 6-31G* basis set. The HOMO energies were $E^{\text{in}}_{\text{HOMO}} = 5.31\,\text{eV}$ and $E^{\text{out}}_{\text{HOMO}} = 5.68\,\text{eV}$. In the PDOS of the molecular region (see Fig. 5.4.2) the highest occupied states are $\Delta E^{\text{in}}_{\text{HOMO}} = 0.51\,\text{eV}$ and $\Delta E^{\text{out}}_{\text{HOMO}} = 0.81\,\text{eV}$ away from the Fermi level. Thus the observed electronic structure of the isolated molecule is also present in the SAM. Obviously no 'SAM effect' of collective electrostatic interaction is responsible for the different transport characteristics. The transport characteristics of the two SAMs is largely determined by the properties of the isolated molecules. Nevertheless, within the last two section, the derived formalism and its implementation were successfully tested.

5.4.3 Preliminary results - the surface DOS and surface band structure of organic monolayers on noble metals

The surface DOS was introduced as a tool to calculate the DOS of a surface. The advantage compared to a 'standard' PDOS is that the surface DOS incorporates the influence of a semi-infinite bulk. One can explicitly define the molecular orbitals the DOS is projected onto in *surfacedos.f90*. As a consequence, the DOS for each layer of the surface region can be resolved as shown in Fig. 5.18. There, the influence of a semi-infinite bulk onto each of the five Au(111) layers and onto the 'N-in' monolayer is shown. One could also calculate the PDOS of specific compounds of the molecular layer (*e.g.* the sulfur orbitals, a certain ring, ...). and explore how those parts are broadened compared to the PDOS of other compounds of the monolayer.

By using the surface DOS we can also calculate the DOS of a layer in the 'true infinite' bulk. The DOS of such a bulk layer of Au(111) is plotted in Fig. 5.18.

[1] We also calculated the Δ_{SCF} values by explicitly substracting an electron and comparing the total energies of the neutral and charged systems. Those values were close to equal for N-in and N-out which is counterintuitive when comparing the molecular HOMO energiess. The reason for this behavior is unknown.

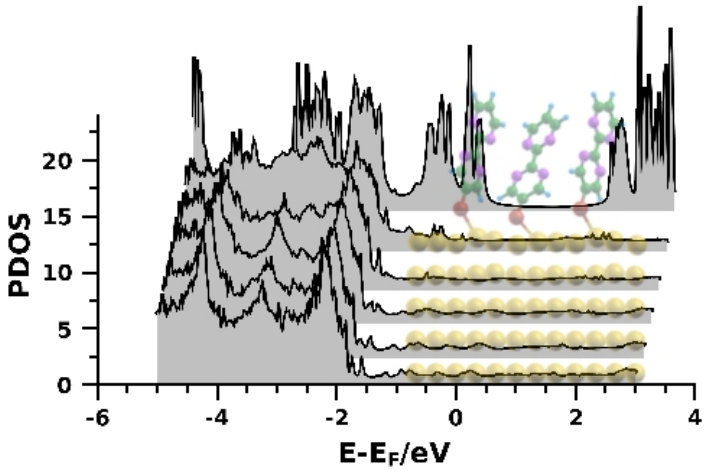

Figure 5.17: The DOS projected onto each layer of Au(111) and the adsorbed N-in monolayer. The PDOS is broadened due to the influence of the semi-infinite bulk. The spectrum is aligned to the Fermi-level.

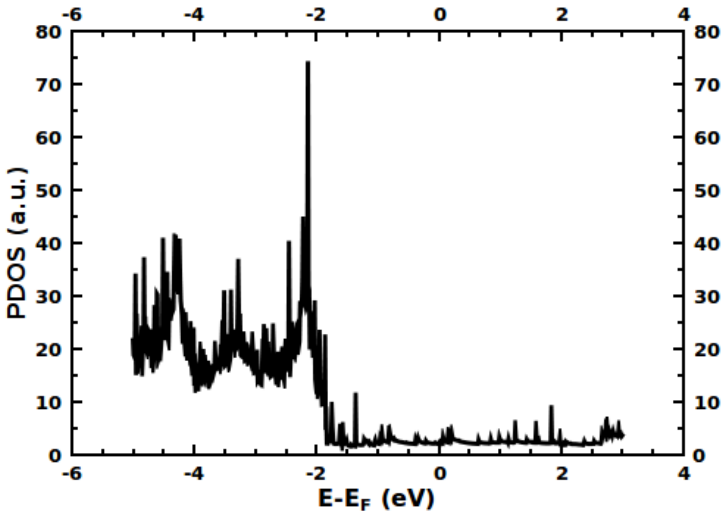

Figure 5.18: The 'true' DOS of a Au(111) bulk layer. The spectrum is aligned to the Fermi-level

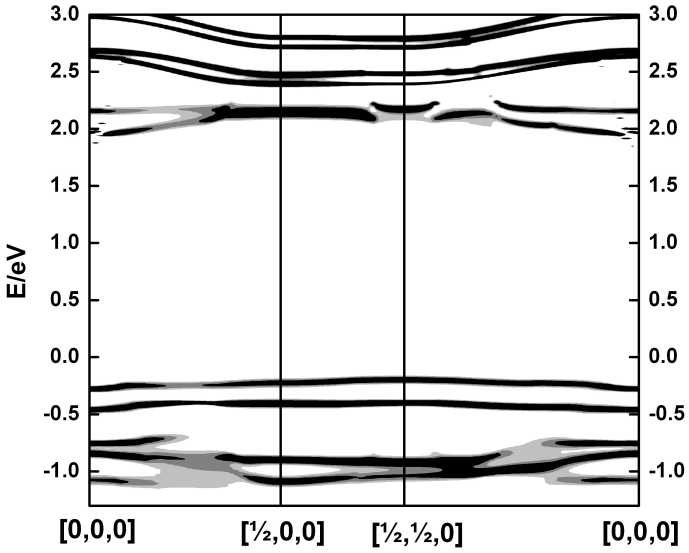

Figure 5.19: The surface band structure for the first occupied and unoccupied states in the 'N-in' monolayer in a contour plot. The spectrum is aligned to the Fermi-level

It was argued that within the surface band structure approach one can obtain a 3D band structure where the z-coordinate is an indicator for the influence of the semi-infinite bulk on the bands. One can plot each k-point's $D(E)$ relationship in a contour plot. Fig. 5.19 shows an overview of the first occupied and unoccupied states in the 'N-in' monolayer in a contour plot. Brighter areas indicate more broadening and hence more influence of the bulk on the electronic structure of the organic layer. Fig. 5.20 shows the HOMO and HOMO-1 bands of the adsorbed 'N-in' monolayer.

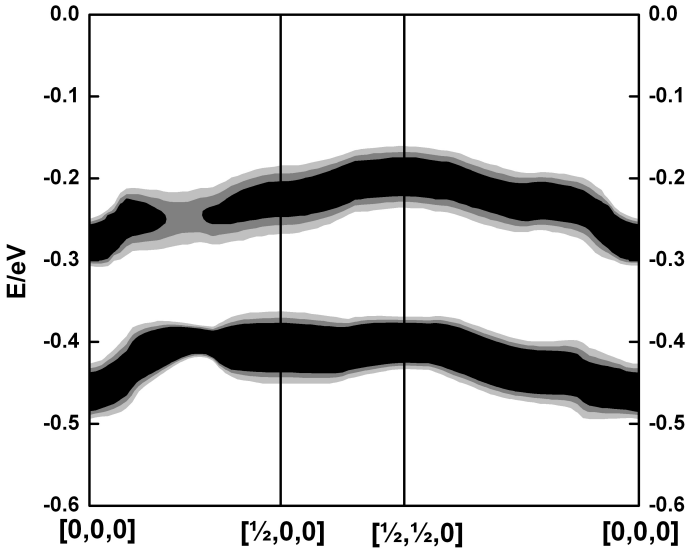

Figure 5.20: The surface band structure for the HOMO and HOMO-1 of the 'N-in' monolayer in a contour plot. The spectrum is aligned to the Fermi-level

Bibliography

[1] Ulrich Horstmann. *Think more, act less : English aphorisms*. Reclam, Stuttgart, [Nachdr.] edition, 2008. 1

[2] J. Christopher Love, Lara A. Estroff, Jennah K. Kriebel, Ralph G. Nuzzo, and George M. Whitesides. Self-Assembled monolayers of thiolates on metals as a form of nanotechnology. *Chemical Reviews*, 105(4):1103–1170, 2005. 1, 18

[3] David A. Egger, Ferdinand Rissner, Gerold M. Rangger, Oliver T. Hofmann, Lukas Wittwer, Georg Heimel, and Egbert Zojer. Self-assembled monolayers of polar molecules on Au(111) surfaces: distributing the dipoles. *Physical Chemistry Chemical Physics*, 2010. 2, 16, 24, 32, 33, 38

[4] H. Sormann and E. Schachinger. Theoretische Festkörperphysik. 4

[5] H. Sormann and E. Schachinger. Bandstrukturmethoden. 4

[6] M. Born and R. Oppenheimer. On the quantum theory of molecules. *Annalen der Physik*, 389(20):457–484, 1927. 4

[7] P. Hohenberg and W. Kohn. Inhomogeneous electron gas. *Physical Review*, 136(3B):B864–B871, 1964. 6

[8] L. H. Thomas. The calculation of atomic fields. *Mathematical Proceedings of the Cambridge Philosophical Society*, 23(05):542, 1927. 6

[9] Walter Ritz. Über eine neue Methode zur Lösung gewisser Variationsprobleme der mathematischen Physik. *Journal für die reine und angewandte Mathematik (Crelles Journal)*, 1909(135):1–61, 1909. 6

[10] W. Kohn and L. Sham. Self-Consistent equations including exchange and correlation effects. *Physical Review*, 140(4A):A1133–A1138, 1965. 6

[11] John Perdew and Yue Wang. Accurate and simple analytic representation of the electron-gas correlation energy. *Physical Review B*, 45(23):13244–13249, 1992. 7

[12] G Kresse. Efficiency of ab-initio total energy calculations for metals and semiconductors using a plane-wave basis set. *Computational Materials Science*, 6(1):15–50, 1996. 7

[13] John Perdew, Kieron Burke, and Matthias Ernzerhof. Generalized gradient approximation made simple. *Physical Review Letters*, 77(18):3865–3868, 1996. 7

[14] J. M Soler and E. Artacho. The SIESTA method for ab initio order-N materials simulation. *Journal of Physics: Condensed Matter*, 14:2745â2779, 2002. 7

[15] Felix Bloch. über die Quantenmechanik der Elektronen in Kristallgittern. *Zeitschrift für Physik*, 52(7-8):555–600, 1929. 8

[16] J. Slater and G. Koster. Simplified LCAO method for the periodic potential problem. *Physical Review*, 94(6):1498–1524, 1954. 9

[17] R. Feynman. Forces in molecules. *Physical Review*, 56(4):340–343, 1939. 9

[18] Tomas Bucko, Jürgen Hafner, and Janos G. Angyan. Geometry optimization of periodic systems using internal coordinates. *The Journal of Chemical Physics*, 122(12):124508, 2005. 9, 25

[19] Richard Mattuck. *A guide to Feynman diagrams in the many-body problem.* Dover Publications, New York, 2nd ed. edition, 1992. 10

[20] Richard Feynman. *The Feynman lectures on physics : the definitive and extended edition*, volume 3. Addison-Wesley, San Francisco Calif. ;Harlow, 2nd ed. edition, 2009. 12

[21] Georg Heimel, Lorenz Romaner, Jean-Luc Bredas, and Egbert Zojer. Interface energetics and level alignment at covalent Metal-Molecule junctions: π-Conjugated thiols on gold. *Physical Review Letters*, 96(19), 2006. 17, 18, 19, 21, 32, 35, 66

[22] H. Ishii, K. Sugiyama, E. Ito, and K. Seki. Energy level alignment and interfacial electronic structures at organic/metal and organiârganic interfaces. *Advanced Materials*, 11(8):605â625, 1999. 17

[23] Georg Heimel, Lorenz Romaner, Egbert Zojer, and Jean-Luc Bredas. The interface energetics of Self-Assembled monolayers on metals. *Accounts of Chemical Research*, 41(6):721–729, 2008. 18, 24, 25, 31

[24] Georg Heimel, Lorenz Romaner, Egbert Zojer, and Jean-Luc Bredas. Toward control of the Metal-Organic interfacial electronic structure in molecular electronics:A First-Principles study on Self-Assembled monolayers of π-conjugated molecules on noble metals. *Nano Letters*, 7(4):932–940, 2007. 18, 19, 21, 24, 25, 29, 31, 35

[25] Seiji Tsuzuki and Hans P. Lüthi. Interaction energies of van der waals and hydrogen bonded systems calculated using density functional theory: Assessing the PW91 model. *The Journal of Chemical Physics*, 114(9):3949, 2001. 24

[26] Norbert Koch. Organic electronic devices and their functional interfaces. *ChemPhysChem*, 8(10):1438–1455, 2007. 24

[27] I. Campbell, S. Rubin, T. Zawodzinski, J. Kress, R. Martin, D. Smith, N. Barashkov, and J. Ferraris. Controlling schottky energy barriers in organic electronic devices using self-assembled monolayers. *Physical Review B*, 54(20):R14321–R14324, 1996. 24, 25

[28] B. de Boer, A. Hadipour, M. M. Mandoc, T. van Woudenbergh, and P. W. M. Blom. Tuning of metal work functions with Self-Assembled monolayers. *Advanced Materials*, 17(5):621–625, 2005. 24, 25

[29] B. H. Hamadani, D. A. Corley, J. W. Ciszek, J. M. Tour, and D. Natelson. Controlling charge injection in organic Field-Effect transistors using Self-Assembled monolayers. *Nano Letters*, 6(6):1303–1306, 2006. 24, 25

[30] P Marmont, N Battaglini, P Lang, G Horowitz, J Hwang, A Kahn, C Amato, and P Calas. Improving charge injection in organic thin-film transistors with thiol-based self-assembled monolayers. *Organic Electronics*, 9(4):419–424, 2008. 24, 25

[31] C. Bock, D. V. Pham, U. Kunze, D. KaÌfer, G. Witte, and Ch. WoÌll. Improved morphology and charge carrier injection in pentacene field-effect transistors with thiol-treated electrodes. *Journal of Applied Physics*, 100(11):114517, 2006. 24

[32] Kyuwook Ihm, Bongsoo Kim, Tai-Hee Kang, Ki-Jeong Kim, Min Ho Joo, Tae Hyeong Kim, Sang Soo Yoon, and Sukmin Chung. Molecular orientation dependence of hole-injection barrier in pentacene thin film on the Au surface in organic thin film transistor. *Applied Physics Letters*, 89(3):033504, 2006. 24

[33] Q. Sun, A. Selloni, and G. Scoles. Electronic structure of Metal/-Molecule//Metal junctions:Â a density functional theory study of the

influence of the molecular terminal group. *The Journal of Physical Chemistry B*, 110(8):3493–3498, 2006. 24

[34] Amir Natan, Yigal Zidon, Yoram Shapira, and Leeor Kronik. Cooperative effects and dipole formation at semiconductor and self-assembled-monolayer interfaces. *Physical Review B*, 73(19), 2006. 24, 27, 33

[35] Maria L. Sushko and Alexander L. Shluger. Intramolecular dipole coupling and depolarization in Self-Assembled monolayers. *Advanced Functional Materials*, 18(15):2228–2236, 2008. 24

[36] G. Kresse and J. Furthmüller. Efficient iterative schemes for ab initio total-energy calculations using a plane-wave basis set. *Physical Review B*, 54(16):11169–11186, 1996. 25

[37] A Kokalj. Computer graphics and graphical user interfaces as tools in simulations of matter at the atomic scale. *Computational Materials Science*, 28(2):155–168, 2003. 25

[38] G Heimel, L Romaner, J Bredas, and E Zojer. Organic/metal interfaces in self-assembled monolayers of conjugated thiols: A first-principles benchmark study. *Surface Science*, 600(19):4548–4562, 2006. 25

[39] Waleed Azzam, Claus Fuxen, Alexander Birkner, Hai-Tao Rong, Manfred Buck, and Christof Wöll. Coexistence of different structural phases in thioaromatic monolayers on Au(111). *Langmuir*, 19(12):4958–4968, 2003. 25

[40] LinJun Wang, Gerold M. Rangger, Lorenz Romaner, Georg Heimel, Tomas Bucko, ZhongYun Ma, QiKai Li, Zhigang Shuai, and Egbert Zojer. Electronic structure of Self-Assembled monolayers on Au(111) surfaces: The impact of backbone polarizability. *Advanced Functional Materials*, 19(23):3766–3775, 2009. 27, 31

[41] D. Cornil, Y. Olivier, V. Geskin, and J. Cornil. Depolarization effects in Self-Assembled monolayers: A Quantum-Chemical insight. *Advanced Functional Materials*, 17(7):1143–1148, 2007. 27, 28

[42] Lorenz Romaner, Georg Heimel, and Egbert Zojer. Electronic structure of thiol-bonded self-assembled monolayers: Impact of coverage. *Physical Review B*, 77(4), 2008. 27, 33, 36

[43] Stephen D. Evans and Abraham Ulman. Surface potential studies of alkyl-thiol monolayers adsorbed on gold. *Chemical Physics Letters*, 170(5-6):462–466, 1990. 28

[44] D. M Alloway, M. Hofmann, D. L Smith, N. E Gruhn, A. L Graham, R. Colorado, V. H Wysocki, T. R Lee, P. A Lee, and N. R Armstrong. Interface dipoles arising from self-assembled monolayers on gold: UV-photoemission studies of alkanethiols and partially fluorinated alkanethiols. *Journal of Physical Chemistry B-Condensed Phase*, 107(42):11690â11699, 2003. 28

[45] Dudi Deutsch, Amir Natan, Yoram Shapira, and Leeor Kronik. Electrostatic properties of adsorbed polar molecules: Opposite behavior of a single molecule and a molecular monolayer. *Journal of the American Chemical Society*, 129(10):2989–2997, 2007. 32, 33

[46] Stephan Kümmel and Leeor Kronik. Orbital-dependent density functionals: Theory and applications. *Reviews of Modern Physics*, 80(1):3–60, 2008. 32

[47] M. Methfessel and A. Paxton. High-precision sampling for brillouin-zone integration in metal s. *Physical Review B*, 40(6):3616–3621, 1989. 35

[48] M. J. Frisch, G. W. Trucks, H. B. Schlegel, G. E. Scuseria, M. A. Robb, J. R. Cheeseman, J. A. Montgomery, Jr., T. Vreven, K. N. Kudin, J. C. Burant, J. M. Millam, S. S. Iyengar, J. Tomasi, V. Barone, B. Mennucci, M. Cossi, G. Scalmani, N. Rega, G. A. Petersson, H. Nakatsuji, M. Hada, M. Ehara, K. Toyota, R. Fukuda, J. Hasegawa, M. Ishida, T. Nakajima, Y. Honda, O. Kitao, H. Nakai, M. Klene, X. Li, J. E. Knox, H. P. Hratchian, J. B. Cross, V. Bakken, C. Adamo, J. Jaramillo, R. Gomperts, R. E. Stratmann, O. Yazyev, A. J. Austin, R. Cammi, C. Pomelli, J. W. Ochterski, P. Y. Ayala, K. Morokuma, G. A. Voth, P. Salvador, J. J. Dannenberg, V. G. Zakrzewski, S. Dapprich, A. D. Daniels, M. C. Strain, O. Farkas, D. K. Malick, A. D. Rabuck, K. Raghavachari, J. B. Foresman, J. V. Ortiz, Q. Cui, A. G. Baboul, S. Clifford, J. Cioslowski, B. B. Stefanov, G. Liu, A. Liashenko, P. Piskorz, I. Komaromi, R. L. Martin, D. J. Fox, T. Keith, M. A. Al-Laham, C. Y. Peng, A. Nanayakkara, M. Challacombe, P. M. W. Gill, B. Johnson, W. Chen, M. W. Wong, C. Gonzalez, and J. A. Pople. Gaussian 03, Revision C.02. Gaussian, Inc., Wallingford, CT, 2004. 38

[49] Ursula Lottermoser, Paul Rademacher, Monika Mazik, and Klaus Kowski. Photoelectron spectra and electronic structures of substituted pyrimidines. *European Journal of Organic Chemistry*, 2005(3):522–531, 2005. 41

[50] C.G. Ning, K. Liu, Z.H. Luo, S.F. Zhang, and J.K. Deng. Electron momentum spectroscopy study on valence electronic structures of pyrimidine. *Chemical Physics Letters*, 476(4-6):157–162, 2009. 41

[51] Navit Dori, Mahesh Menon, Lennart Kilian, Moritz Sokolowski, Leeor Kronik, and Eberhard Umbach. Valence electronic structure of gas-phase 3,4,9,10-perylene tetracarboxylic acid dianhydride: Experiment and theory. *Physical Review B*, 73(19), 2006. 41

[52] T. Körzdörfer, S. Kümmel, N. Marom, and L. Kronik. When to trust photoelectron spectra from Kohn-Sham eigenvalues: The case of organic semiconductors. *Physical Review B*, 79(20), 2009. 41

[53] Mads Brandbyge, Jose-Luis Mozos, Pablo Ordejon, Jeremy Taylor, and Kurt Stokbro. Density-functional method for nonequilibrium electron transport. *Physical Review B*, 65(16), 2002. 43, 54, 70

[54] D.A. Ryndyk, R. Gutierrez, B. Song, and G. Cuniberti. *Energy Transfer Dynamics in Biomaterial Systems*, pages 213–335. 2008. 43, 54, 55

[55] Supriyo Datta. *Quantum transport : atom to transistor*. Cambridge University Press, Cambridge UK ;;New York, 2005. 43, 51, 56, 57

[56] Supriyo Datta. Ece 659 quantum transport: Atom to transistor, Jan 2009. 43

[57] Supriyo Datta. Quantum transport: Atom to transistor (spring 2004), Aug 2006. 43

[58] Supriyo Datta. Electrical resistance: an atomistic view. *Nanotechnology*, 15(7):433–451, 2004. 43

[59] M. Paulsson. Non equilibrium green's functions for dummies: Introduction to the one particle negf equations, 2002. 43

[60] Magnus Paulsson, Ferdows Zahid, and Supriyo Datta. *Resistance of a Molecule*. April 2003. 43

[61] Ferdows Zahid, Magnus Paulsson, and Supriyo Datta. *Electrical Conduction through Molecules*. July 2003. 43

[62] MPL Sancho, JML Sancho, and J Rubio. Highly convergent schemes for the calculation of bulk and surface Green-functions. *Journal of physics F-metal physics*, 15(4):851–858, 1985. 60

[63] Marco Nardelli. Electronic transport in extended systems: Application to carbon nanotubes. *Physical Review B*, 60(11):7828–7833, 1999. 60

[64] Yong-Hoon Kim, Seung Soon Jang, and William A. Goddard. Conformations and charge transport characteristics of biphenyldithiol self-assembled-monolayer molecular electronic devices: A multiscale computational study. *The Journal of Chemical Physics*, 122(24):244703, 2005. 66, 67, 68, 69